SOIL MOISTURE RETRIEVAL USING SLICED REGRESSION INVERSION TECHNIQUE

A THESIS

submitted by

SIDDHANT GAUTAM

for the award of the degree

of

MASTER OF SCIENCE

(by Research)

DEPARTMENT OF ELECTRICAL ENGINEERING
INDIAN INSTITUTE OF TECHNOLOGY MADRAS.

SEPTEMBER 2020

THESIS CERTIFICATE

This is to certify that the thesis titled **Soil Moisture Retrieval Using Sliced Regression Inversion Technique**, submitted by **Siddhant Gautam**, to the Indian Institute of Technology, Madras, for the award of the degree of **Master of Science**, is a bonafide record of the research work done by him under our supervision. The contents of this thesis, in full or in parts, have not been submitted to any other Institute or University for the award of any degree or diploma.

Prof. Uday K. Khankhoje
Research Guide
Assistant Professor
Dept. of Electrical Engineering
IIT-Madras, 600 036

Place: Chennai

Date: 23rd September 2020

ACKNOWLEDGEMENTS

IIT Madras has been a wonderful place to be for the past three years. Here I had the privilege of meeting some of the most beautiful persons who have contributed to making this a great experience and have enabled me to grow into a mature researcher.

I wish to express my deepest gratitude to my thesis advisor Prof. Uday Khankhoje for his guidance throughout my research and for encouraging me to pursue the field of microwave remote sensing. This project would not have been possible without his constant support and motivation. His courses Linear Algebra and Computational Electromagnetics provided me with a good background in applied mathematics and scientific computing that set the pace for my research work. Through this project, I got introduced to the research methodology and hence I learned how to tackle research problems with the right mindset. It also enabled me to build up my computational skills, especially in C++, MATLAB, and Python. Through the regular assistance of my faculty advisor Prof. Uday Khankhoje, I was able to perform well consistently and consequently, I was able to able to publish and present my research work in a peer-reviewed conference titled Progress in Electromagnetic Research Symposium (PIERS-2019) held in Rome, Italy from June 17-20, 2019.

Taking various mathematical courses at IIT-M helped me in building a strong foundation in mathematical and computing science and exposed me to enough mathematical rigor to tackle challenging research problems in the domain of scientific computing. Alongside my research, my duties as a teaching assistant every semester was a very good learning experience where I also had the privilege of being a teaching assistant for the MOOC: “Computational Electromagnetics”, taught by Professor Uday Khankhoje. This TA work combined with my courses and research taught me the importance of time management and thus enabled me to grow into a mature researcher.

I would like to acknowledge Space Applications Centre (SAC), Indian Space Research Organisation for their funding to the project, and our collaborator Dharmendra Kumar Pandey for providing us with the experimental data and for helping out with

useful suggestions. I am also grateful to the members of my general test committee Professors Harishankar Ramachandran, Shanti Bhattacharya, and Vaibhav Madhok for providing valuable insights into the project and for overseeing my progress during my time here. I would also like to thank my friends: Rudra, Sujay, Shahrukh and Disha and labmates: Sakees, Karteek, Sriram, Aggraj, Yaswanth, Yash, Prajosh, Chandan, Ankit, Ayushi, and Sowjanya for helping me out in my work and providing me with good company throughout my graduate studies at IITM. I thank our lab staff Jegan, who has also been a great help in carrying out the essential tasks involved with our lab. Finally, I wish to acknowledge the support and great love of my parents and my brother, who kept me going. This work would not have been possible without their emotional support.

ABSTRACT

KEYWORDS: soil moisture, data cube, regression, bins, least squares

Soil moisture retrieval is one of the most important aspects of Earth science observation where it can be used to predict various climate events. Several empirical and theoretical approaches have been proposed in the past for soil moisture retrieval. We propose a novel soil moisture retrieval algorithm based on electromagnetic scattering model. Being a physics-based model, our sliced regression inversion (SRI) algorithm works for a wide range of geophysical parameters without any dependence on previously acquired datasets. In other words, our SRI algorithm has a wide range of applicability in terms of the physical parameters that it can invert. As a result, it is expected to produce 100 $\%$ inversion rate within the validity range which is an added advantage of the proposed technique. Our SRI technique builds on and improves the lookup table approach by approximating the relationship between radar backscattering coefficients and the underlying physical variables by piece-wise linear fits. The regression coefficients from the piece-wise fits are used to solve a least squares equation to estimate the soil-vegetation parameters including soil moisture.

The Improved Integral Equation Model (I^2EM) is used as the forward scattering model to calculate the radar backscatter from scattering for bare soils. We extend this forward model to include depth-dependent moisture by calculating the Fresnel reflection coefficients for a heterogeneous soil profile. The effect of vegetation scattering are included by modeling the electromagnetic interactions between the individual plants. This is done by modeling the vegetation as a collection of randomly oriented dielectric cylinders and then summing contributions from individual scatterers with an appropriate probability density function. We also present the time series based approach to retrieved soil moisture in case of vegetated lands. Later we validate our model with experimental data acquired from ALOS-PALSAR and SENTINEL satellites and retrieve soil moisture with the best possible accuracy (root mean squared error) of 0.06 $cm^3/cm^3$for bare

soil and 0.14-0.18 $cm^3/cm^3$for vegetated lands. For retrievals with the synthetic test datasets, we report an accuracy of 0.05 $cm^3/cm^3$for bare soil and 0.06 $cm^3/cm^3$for vegetated lands using L and S band data. We also show that our algorithm performs better than both the SMART inversion model as well as the lookup table approach. We report the best accuracy while working with fusing the co-polarized and cross-polarized backscatter data from two different bands with an appropriate explanation.

TABLE OF CONTENTS

LIST OF TABLES

LIST OF FIGURES

ABBREVIATIONS

IITM	Indian Institute of Technology, Madras
SRI	Sliced Regression Inversion
IEM	Integral Equation Model
I^{2}EM	Improved Integral Equation Model
LUT	lookup Table

NOTATION

h	RMS Surface Height, cm
l	Surface Correlation Length, cm
mv	Soil Moisture Content, cm^3/cm^3
vm	Vegetation Moisture Content, cm^3/cm^3

CHAPTER 1

INTRODUCTION

Soil moisture refers to the volume fraction of water present in the top few centimetres of the Earth's surface. Soil moisture information is used by climatologists, agriculture scientists, etc. in predicting floods, droughts, crop monitoring, and weather forecasting. Hence, it is important to retrieve soil moisture. Soil moisture retrieval is the process of estimating the moisture content of the soil (cm^3/cm^3) from the backscattering coefficient taken by a synthetic aperture radar. Active microwave remote sensing through the use of synthetic aperture radar (SAR) offers a high spatial resolution in estimating soil moisture and can provide information about the moisture both on the soil surface and several centimetres below it depending on the operating wavelength of the radar. Radiometer based estimates of soil moisture also exists but they have very limited spatial resolution. As a result, there has been a significant effort in estimating soil moisture using truck mounted scatterometers (Ulaby, 1974; Ulaby *et al.*, 1990), air (Rosen *et al.*, 2006; Allen *et al.*, 2010; Chapin *et al.*, 2012; Tabatabaeenejad *et al.*, 2014) or spaceborne (Dobson and Ulaby, 1986*a*; Entekhabi *et al.*, 2010; Kerr *et al.*, 2001) microwave synthetic aperture radar (SAR).

The radar backscattering coefficient, which is the ratio of received power and transmitted power by a SAR in the direction coming back to the radar, is a function of electrical and geometrical properties of soil and vegetation and thus it can be used for the purpose of soil moisture retrieval. Because of the high dielectric contrast between dry soil and the water, the complex permittivity of soil is affected by the amount of moisture present in the top layer, which in turn influences the radar backscatter. Other factors that influence the backscatter include surface roughness, heterogeneous moisture distribution (Khankhoje *et al.*, 2012; Konings *et al.*, 2014), amount of vegetation (Bindlish and Barros, 2001; Alemohammad *et al.*, 2019; Burgin *et al.*, 2016), etc. Thus the task of retrieving soil moisture is not straightforward as it is made complicated by the dependence of backscatter on various parameters.

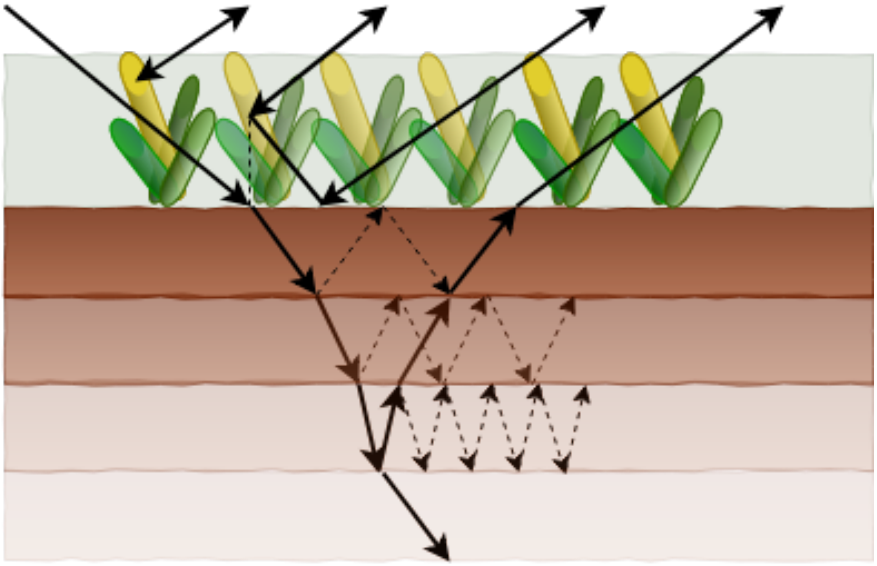

Figure 1.1: Scattering from a rough surface covered with vegetation

1.1 Literature Survey

Several approaches in the past have been proposed for soil moisture retrieval purposes from radar backscatter data which can be classified into empirical, semi-empirical or physics-based/theoretical models (Oh *et al.*, 1992; Dubois *et al.*, 1995; Shi *et al.*, 1997; Quesney *et al.*, 2000; Moghaddam *et al.*, 2000; De Roo *et al.*, 2001; Zribi and Dechambre, 2003; Dobson *et al.*, 1985; Peplinski *et al.*, 1995; Hajnsek *et al.*, 2003; Dave *et al.*, 2019; Kim *et al.*, 2017; Narvekar *et al.*, 2015; Kerr *et al.*, 2012; Njoku and Li, 1999; Entekhabi *et al.*, 2004; Dobson and Ulaby, 1986*a*). Since empirical models are based on specific datasets, they have limited guarantee and site specific validity even though they are easier to derive. On the other hand, the semi-empirical models use part of experimental/simulated datasets in addition to a theoretical model. Whereas the theoretical models are based on electromagnetic scattering models and hence they work for a large range of soil and vegetation parameters and hence are not restricted to any particular site. Since they are based on physics models, the theoretical approaches are quite complicated due to involvement of several parameters and thus their inversion is difficult. However they offer the advantage of greater generality and wider applicability, provided they can be efficiently implemented.

In some empirical models, a linear relationship is obtained between the soil moisture

and the backscattering coefficient to retrieve the volumetric soil moisture (Jackson and Schiebe, 1993; Schneider and Oppelt, 1998; Quesney *et al.*, 2000). Earlier approaches used single frequency and single polarization data to retrieve soil parameters (Wang *et al.*, 1986; Dobson and Ulaby, 1986*b*). However, it was observed that more information from SAR data i.e. multiple polarizations lead to better accuracy in the estimation of soil moisture content. As a result, dual polarizations (Shi *et al.*, 1997; Dubois *et al.*, 1995) as well as triple-polarization (Oh *et al.*, 1992) backscatter data were used to retrieve soil moisture. In order to further improve the accuracy of soil moisture retrieval, various time-series approaches were proposed that used the information about the prior estimate of soil moisture(Kim and van Zyl, 2009; Ulaby *et al.*, 1981; Wagner and Scipal, 2000; Kim *et al.*, 2011; Ouellette *et al.*, 2017; Al-Khaldi *et al.*, 2019). It is based on the fact that the moisture content of soil changes with time due to atmospheric conditions while the surface geometrical properties remain the same. Using experimental data, the retrieval of soil moisture under vegetation canopies has been studied (Moghaddam *et al.*, 2000; De Roo *et al.*, 2001). Recently, convolutional neural networks (CNNs) have also been quite popular for retrieval of soil moisture by establishing a statistical relationship between the soil parameters and the backscatter to retrieve soil moisture (Rodríguez-Fernández *et al.*, 2015; Wang *et al.*, 2019). Various studies have also been carried out to find out a successful relation between the soil moisture and its complex permittivity some of which include (Topp *et al.*, 1980; Hallikainen *et al.*, 1985).

A key task in remote sensing problems is to model the electromagnetic scattering from a random rough surface. First order small-perturbation model (Rice, 1951; Beckmann and Spizzichino, 1987) has been proposed in the past to describe scattering from slightly rough surfaces. But it applies only to surfaces whose roughness is small and thus it has limited scope. Recently Integral Equation Model (Fung *et al.*, 1992) and its improved version (Fung *et al.*, 2002) has been proposed which can model the backscatter from the soil surface accurately for any range of surface roughness. Recently, more advanced versions of IEM known as Advanced IEM (Chen *et al.*, 2003), (Yang *et al.*, 2017) has been proposed that takes into effect the multiple scattering terms which contribute significantly to the cross-polarized backscatter.

The improved integral equation model I^2EM treats soil as a homogeneous half space and moisture is assumed to be constant with depth. However it is observed that soil dries from top after rain and there is a need to model this depth dependency of mois-

ture. The modified IEM (Fung *et al.*, 1996) assumes a vertical soil moisture profile by incorporating a physical dielectric gradient (Brekhovskikh, 2012) into the model. We extend our forward model by incorporating this depth-dependent moisture by modifying the reflection coefficients in the I^{2}EM. To model scattering through vegetation, a water cloud model(Attema and Ulaby, 1978) for the vegetation has been proposed in the past with its parameters empirically determined from the data(Bindlish and Barros, 2001). Since the parameters of this model are empirically determined, it can't be generalized to all vegetation. In our work, we use the dielectric cylinder approach (Arii, 2009; van Zyl, 2011), in which vegetation is modeled as a collection of lossy dielectric scatterers. Radar backscatter is calculated by considering the contribution of scattering from multiple paths through the vegetation to the final backscatter direction.

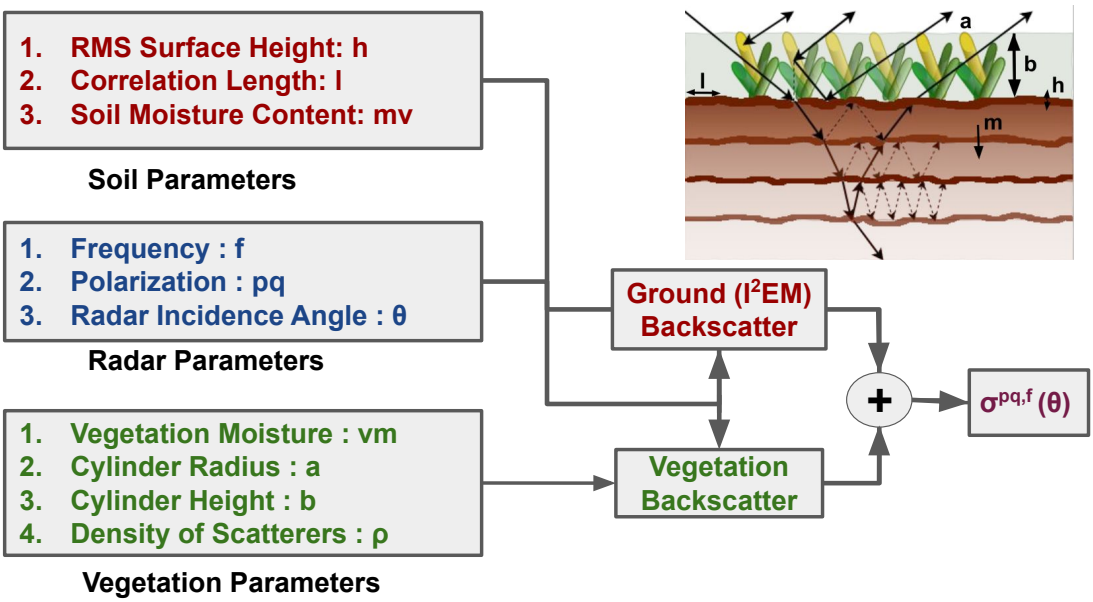

Figure 1.2: Block Diagram of Forward Model

1.2 Proposed Technique

In this thesis, a novel soil moisture retrieval technique called the Sliced Regression Inversion Algorithm is proposed which retrieves soil moisture from both bare soil as well as vegetated lands. It uses the Improved Integral Equation Model (Fung *et al.*, 2002) and the dielectric cylinder approach (Arii, 2009; van Zyl, 2011) as the forward model for bare soil and vegetated lands. A schematic of the overall forward model used and the parameters involved is shown in Figure 1.2. Using the above forward models, the

data cube is generated using roughness parameters along with soil and vegetation parameters. A data cube corresponds to a particular combination of radar frequency and polarization and we generate six such data cube in case of NISAR operating bands: [HH,L], [VV,L],[HV,L], [HH,S], [VV,S], [HV,S]. Each data cube is divided into bins or slices and a linear relation is fit between the input (soil moisture, root mean squared surface height, correlation length, etc.) and output (backscattering coefficients) parameters within each bin to get a set of regression coefficients. Given the radar measurements, we estimate the soil moisture by finding the optimal bin from the knowledge of regression coefficients. We solve a bounded least squares equation to find the bin which gives the lowest residual error and retrieve the corresponding value of soil moisture.

We know that the I2EM has its own range of validity and boundary conditions in terms of surface roughness parameters. Since the SRI algorithm uses I2EM to generate the backscatter data for bare soil, the validity range and limitations of SRI algorithm directly depends on those of the I2EM.

1.3 Relevance to Upcoming Missions

Various global missions have been launched that seeks to estimate the soil moisture using active microwave sensors, especially at L, S, and C-band. This includes the Soil Moisture Active Passive (SMAP) mission (Entekhabi *et al.*, 2010) which was launched in 2015, Soil Moisture Ocean Salinity (SMOS)(Kerr *et al.*, 2001) and a few others (Kerr *et al.*, 2012; Konings *et al.*, 2014). Our SRI algorithm finds application in the upcoming NASA-ISRO Synthetic Aperture Radar (NISAR) mission (Rosen *et al.*, 2017), which is a collaboration between the National Aeronautics and Space Administration (NASA) and the Indian Space Research Organisation (ISRO). The objective of the mission is to retrieve soil moisture on a global scale using L and S-band. By fusing scattering models appropriate to each band, it is expected that high spatial resolution soil moisture retrieval at meter scale and higher accuracy in physical parameter retrievals than with a single band can be achieved; this is shown in our results subsequently.

1.4 Thesis Organization

The flow of this thesis is organized as follows. In Chapter 2, we present the mechanism of radar scattering from bare soil surface. Next, we present the details of vegetation modeling and the corresponding calculation of vegetation backscatter in Chapter 3.The details of the sliced regression inversion algorithm are presented in Chapter 4. Subsequently, in Chapter 5, we present the results of applying the algorithm on synthetic and experimentally obtained datasets, along with comparisons with the lookup table approach. We also provide a detailed analysis of the results in the same section. In Chapter 6, various time series approaches to retrieve soil moisture has been discussed. Finally, we conclude in Section 7 with a summary of the method and results.

CHAPTER 2

BARE SOIL SCATTERING

2.1 Introduction

Radar backscatter from the ground surface is a result of both surface as well as volume scattering. The surface scattering is generated due to the random nature of the shape of air-soil interface and both single as well as multiple scattering events give rise to the surface scattering. Single scattering occurs from the facets whose normal is oriented towards the radar whereas multiple scattering takes place from reflections by multiple facets. There are random height deviations above the mean height of the surface roughness which needs to be modeled by a random process. This statistical nature of rough surface and its complex shape makes the task of modeling surface scattering difficult. In this chapter, we shall discuss an electromagnetic model called the Integral Equation Model Fung *et al.* (1992) which models backscattering from a random rough surface.

2.2 Surface Parameters

Electromagnetic wave scattering from a bare soil which has a randomly rough surface is affected by soil roughness and the permittivity of the soil. Any rough surface can be described in terms of statistical distribution of which Gaussian and exponential are the most popular ones. The soil roughness can be characterized by two statistical parameters which are root mean squared (rms) surface height (h) and the soil correlation length (l). For a rough surface with probability density function $p(z)$ and the height $z(x, y)$ above the mean, the rms height for a zero mean surface is given by:

$$h = \left[\int_{-\infty}^{\infty} z^2 p(z)\, dz \right]^{1/2} \tag{2.1}$$

The surface correlation function defined by (Ulaby *et al.*, 2014)

$$\rho(\zeta) = \langle z(x, y) z(x', y') \rangle \tag{2.2}$$

is a measure of the degree of correlation between the surfaces at location (x, y) and (x', y') with $\zeta = \sqrt{(x-x')^2 + (y-y')^2}$ distance between them. We can now define the correlation length l as the separation $\zeta = l$ for which

$$\rho(\zeta) = e^{-1} \tag{2.3}$$

The exponential correlation function $\rho_e(\zeta)$ and the Gaussian correlation function $\rho_G(\zeta)$ are defined as (Fung *et al.*, 1992)

$$\rho_e(\zeta) = \exp\left(-|\zeta|/l\right) \tag{2.4}$$

$$\rho_G(\zeta) = \exp\left(-\zeta^2/l^2\right) \tag{2.5}$$

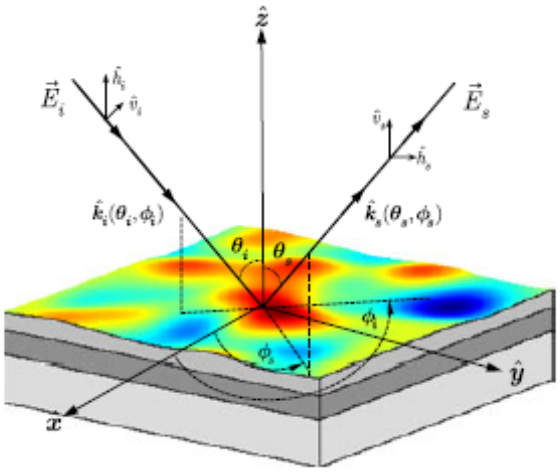

Figure 2.1: Geometry of rough surface scattering (Credits: (Yang *et al.*, 2017))

In the backscattering direction, the following relation holds

$$\theta_s = \pi - \theta_i, \phi_s = \phi_i + \pi \tag{2.6}$$

where θ_i is the incident elevation angle ϕ_i is the incident azimuth angle θ_s is the scattered elevation angle ϕ_s is the scattered azimuth angle

2.3 Improved Integral Equation Model

According to criteria established by Peake and Oliver (Peake and Oliver, 1971), a surface can be called rough if its root means squared (rms) height h satisfies the relation $h > \lambda/4\cos\theta$, where λ is the wavelength and θ is the incidence angle of radar wave. The Small Perturbation Model (SPM) (Rice, 1951) can be used to describe scattering for smooth surfaces for which $h < \lambda/25\cos\theta$.

Kirchhoff approximation (Ulaby, 1982; Tsang *et al.*, 1985; Fung, 1994; Kong, 2001) has been applied to describe random rough surface scattering for surfaces with large surface curvature. Small slope approximation (SSA) (Broschat, 1993; Voronovich, 1994; Irisov, 1997; Johnson, 2002) is another method that describes wave scattering from rough surfaces with wide variety of roughness values. However, the integral equation model (IEM) (Fung, 1994; Fung *et al.*, 1992) applies to both smooth and rough surface scattering and when the surface is smooth enough ($kh < 0.3$), its solution is in agreement with SPM.

The original IEM (Fung *et al.*, 1992) considers a simplifying assumption for the phase of Green's function by eliminating it in the single scattering model. However, the the improved integral equation model (Fung *et al.*, 2002) removes the simplifying assumption on the phase of Green's function and still gives the backscatter in algebraic form which includes the single and multiple scattering terms.

An extended version of IEM known as the Advanced Integral Equation Model (AIEM) (Chen *et al.*, 2000, 2003; Fung and Chen, 2004; Wu and Chen, 2004; Fung *et al.*, 2010) is a very accurate model in predicting scattering from random rough surface. AIEM contains a more complete expression of the single-scattering terms. The multiple scattering terms which consists of Kirchhoff, complementary and the cross components are rederived after including the spectral representation of Green's function. (Yang *et al.*, 2017; Yang and Chen, 2019) consider new expressions for multiple scattering in AIEM up to second order which includes the upward and downward propagating waves.

In this thesis, we use the improved integral equation model(Fung *et al.*, 2002) to generate backscatter for the bare soil case. For a given rough surface, the improved integral equation model generates backscatter σ for any combination of transmit-receive

polarization for a radar operating at wavelength λ and incidence angle θ. According to I2EM, the backscattering coefficient can be written as

$$\sigma_{qp} = S(\theta, \theta_s)\frac{k^2}{2}\exp\left[-\sigma^2(k_z^2 + k_{sz}^2)\right]\sum_{n=1}^{\infty}\sigma^{2n}|I_{qp}^n|^2\frac{W^{(n)}(k_{sx}-k_x, k_{sy}-k_y)}{n!} \quad (2.7)$$

where k is the wavenumber in the medium above the surface with $k_x = k\sin\theta\cos\phi$, $k_y = k\sin\theta\sin\phi$, and $k_z = k\cos\theta$. $S(\theta, \theta_s)$ is the bistatic shadowing function (Sancer, 1969) and $W^{(n)}$ is the Fourier transform of the nth power of the surface correlation function $\rho(r, \varphi)$ given by

$$W^n(K, \phi) = \int_0^{2\pi}\int_0^{\infty}[\rho(r,\varphi)]^n e^{jKr\cos(\varphi-\phi)} r\, dr\, d\varphi \quad (2.8)$$

$$I_{qp}^n = (k_{sz}+k_z)^n f_{qp}\exp\left(-\sigma^2 k_z k_{sz}\right) + \frac{(k_{sz})^n F_{qp}(-k_x,-k_y) + (k_z)^n F_{qp}(-k_{sx},-k_{sy})}{2} \quad (2.9)$$

The field coefficients f_{pq} and F_{pq} are functions of the Fresnel reflection coefficient (R_h, R_v). They are a function of the soil permittivity ϵ_r which is determined by the amount of soil moisture. The expressions for field coefficients f_{qp}, F_{qp} are

$$f_{vv} = \frac{2R_{\|}}{\cos\theta + \cos\theta_s}[\sin\theta\sin\theta_s - (1+\cos\theta\cos\theta_s)\cos(\phi_s - \phi)] \quad (2.10)$$

$$f_{hh} = -\frac{2R_{\perp}}{\cos\theta + \cos\theta_s}[\sin\theta\sin\theta_s - (1+\cos\theta\cos\theta_s)\cos(\phi_s - \phi)] \quad (2.11)$$

where $R_{\|}$ and $R_{\perp}$ are the Fresnel reflection coefficients, and

$$R_{\|} = \frac{\epsilon_r - \sqrt{\mu_r\epsilon_r - \sin^2\theta}}{\epsilon_r + \sqrt{\mu_r\epsilon_r - \sin^2\theta}} \quad \text{and} \quad R_{\perp} = \frac{\mu_r - \sqrt{\mu_r\epsilon_r - \sin^2\theta}}{\mu_r + \sqrt{\mu_r\epsilon_r - \sin^2\theta}} \quad (2.12)$$

$$F_{vv}(-k_x, k_y) = \frac{(\mu_r \epsilon_r - \sin^{\theta} - \epsilon_r \cos^{\theta}(1 + R_{\|})^2}{(\epsilon_r \cos\theta)^2 \cos\theta_s} \cdot \sin\theta[\sin\theta_s - \sin\theta\cos(\phi_s - \phi)] \quad (2.13)$$

$$F_{hh}(-k_x, k_y) = -\frac{(\mu_r \epsilon_r - \sin^{\theta} - \mu_r \cos^{\theta}(1 + R_{\perp})^2}{(\mu_r \cos\theta)^2 \cos\theta_s} \cdot \sin\theta[\sin\theta_s - \sin\theta\cos(\phi_s - \phi)] \quad (2.14)$$

where σ is the rms surface height, ϵ_r and μ_r is the relative permittivity and permeability of soil respectively. k is the wave-number of radar incident wave, pq is the transmit-receive polarization, θ and θ_s are the incidence and scattering elevation angles respectively. ϕ and ϕ_s are the incidence and scattering elevation angles respectively.

The complex permittivity can be calculated from soil moisture content using the Hallikainen dielectric model (Hallikainen *et al.*, 1985) as follows:

$$\epsilon = (a_0 + a_1 S + a_2 C) + (b_0 + b_1 S + b_2 C)mv + (c_0 + c_1 S + c_2 C)mv^2 \quad (2.15)$$

where S and C are the sand and clay textural component of the soil (in percent by weight) and the coefficients a, b, c are the coefficients which are functions of radar operating frequency.

2.4 Effects of Depth Dependent Moisture

In nature, the soil properties vary not only over the surface but with depth as well. This variation of the water content over depth within a soil-profile is called the soil moisture profile. Due to soil heterogeneity, the distribution of amount of water varies with depth. The soil moisture profile has a strong influence on the complex permittivity of the soil and hence the backscatter from the soil surface. The Improved Integral Equation Model(I^2EM) assumes the soil profile to be homogeneous, i.e. moisture is constant con-

cerning depth. Instead, we model the soil profile as a piece-wise constant, multilayer dielectric surface in which the field encounters multiple reflections as shown in Figure 2.2 due to varying soil permittivity. For this purpose, we assume an exponentially varying dielectric profile (Fung *et al.*, 1996; Brekhovskikh, 2012) for the soil, whose expression is given by

$$\epsilon_r(z) = 1 + \frac{2(\epsilon_{r_0} - 1)}{1 + e^{-mz}}, \ z \geq 0 \tag{2.16}$$

where m is the transition rate factor and ϵ_{r_0} is the dielectric constant of the topmost layer. To account for the depth dependence, we update the reflectivities in the I^{2}EM with the effective Fresnel reflection coefficients of scattering from the heterogeneous soil profile.

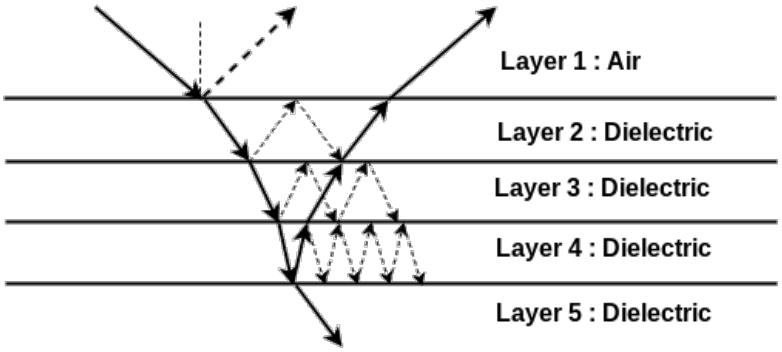

Figure 2.2: Multiple radar reflections from dielectric layers

The reflection coefficient from a layered medium with a flat interface can be calculated for the given permittivity profile using the transfer matrix method (Hulst and van de Hulst, 1981) as shown below

$$\underbrace{\begin{pmatrix} e^{-jk_i d_i} & 0 \\ 0 & e^{jk_i d_i} \end{pmatrix}}_{\mathbf{\Phi_i}} \underbrace{\begin{pmatrix} E_i^- \\ E_i^+ \end{pmatrix}}_{\mathbf{E_i}} = \frac{1}{T_{i,i+1}} \underbrace{\begin{pmatrix} 1 & R_{i,i+1} \\ R_{i,i+1} & 1 \end{pmatrix}}_{\mathbf{TF_i}} \underbrace{\begin{pmatrix} E_{i+1}^- \\ E_{i+1}^+ \end{pmatrix}}_{\mathbf{E_{i+1}}} \tag{2.17}$$

where E_i^- and E_i+ are the electric fields in medium i propagating downwards and upwards respectively. R_{ij} and T_{ij} are the reflection and transmission coefficients of a wave travelling from medium i to j, given by

$$R_{ij} = \frac{n_i \cos\theta_i - n_j \cos\theta_j}{n_i \cos\theta_i + n_j \cos\theta_j} \qquad T_{ij} = \frac{2n_i \cos\theta_i}{n_i \cos\theta_i + n_j \cos\theta_j}$$

where θ_i and θ_j are the incidence and refractive angle at the interface. The refractive angle can be determined from Snell's law of refraction as:

$$\theta_j = \sin^{-1}\left(\frac{n_i}{n_j}\right)\sin\theta_i \tag{2.18}$$

Writing the electric field equation for all the layers i.e. from $i = 1$ to $n - 1$, the electric field at the topmost layer $\mathbf{E_1}$ can be expressed in terms of the field at the bottom layer $\mathbf{E_n}$ as follows:

$$\mathbf{E_1} = \mathbf{\Phi_1}^{-1}\mathbf{TF_1}\mathbf{\Phi_2}^{-1}\mathbf{TF_2}\cdots\mathbf{\Phi_{n-1}}^{-1}\mathbf{TF_{n-1}}\mathbf{E_n}$$

The above equation can be simplified by writing the matrix product into a single matrix as:

$$\begin{pmatrix} E_1^- \\ E_1^+ \end{pmatrix} = \begin{pmatrix} a & b \\ c & d \end{pmatrix} \begin{pmatrix} E_n^- \\ E_n^+ \end{pmatrix} \tag{2.19}$$

The boundary condition states that the electric field is not reflected at the bottom-most interface, thus $E_n^+ = 0$. Applying this boundary conditions to the above equation, we get

$$E_1^- = aE_n^- \quad E_1^+ = cE_n^- \tag{2.20}$$

The total reflection coefficient, which is the ratio of reflected field to incident field, can now be written as

$$\boxed{R_{total} = \frac{E_1^+}{E_1^-} = \frac{c}{a}} \tag{2.21}$$

This value of modified reflection coefficient is used in place of the standard formulae in the original I^{2}EM to generate the modified radar backscatter.

CHAPTER 3

VEGETATION SCATTERING

3.1 Introduction

Soil moisture estimation from vegetated lands is a very challenging task as the modelling of vegetation scattering is not very straightforward. Most of the earth's surface is covered with some form of vegetation, so there is a need to develop a model that can efficiently calculate the radar backscatter from vegetation and retrieve the soil moisture. In this thesis, we present a single layer vegetation scattering model (van Zyl, 2011), (Arii, 2009) that can simulate the radar backscattering from primary scatterers such as stalks, stems, etc.

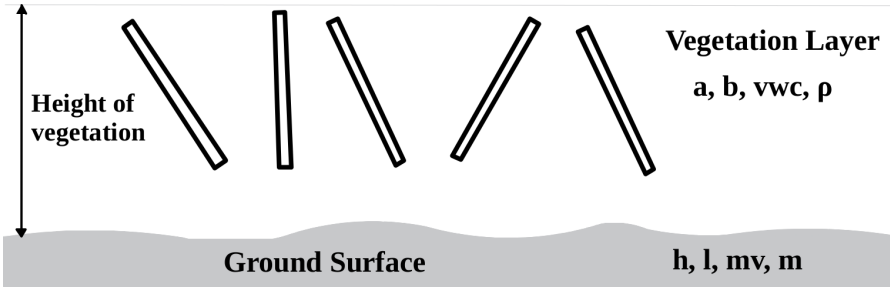

Figure 3.1: Vegetation modeled as collection of randomly oriented dielectric cylinders

There are two types of interfaces - vegetation layer and ground layer that contributes to the final backscatter wave as shown in Figure 3.1. The vegetation is characterized by the layer height b, cylinder radius a, vegetation moisture vm, and density ρ. Similarly, the scattering from ground surface is influenced by soil dielectric constant ϵ_g, root mean squared surface height h, surface correlation length l.

To calculate the vegetation backscattering, vegetation is modeled as a collection of randomly oriented geometrical structures functioning as dielectric scatterers (Figure 3.1). The spatial distribution is dictated by a probability distribution function $p(\theta_c, \phi_c)$ and this is done in a way to mimic the true geometrical orientation of the vegetation. For the modeling of crops, we assume that vegetation is single layer of dielectric cylinders

whose spatial distribution is governed by cosine squared probability density function about the vertical (Arii, 2009).

The radar backscattering coefficient, σ, over vegetated terrain is a function of the electrical and geometric properties of the soil and vegetation cover, as well as radar parameters such as the frequency, polarization, and incidence angle. In this model, there are four different scattering paths to be considered for the total scattering (Freeman and Durden, 1998). These consists of vegetation scattering, direct backscattering from the ground surface and double bounce reflection, each of which is discussed below in detail. The various scattering paths that contribute to σ from a single layer of vegetation are shown in Figure 3.2, and enumerated as follows:

1. Scattering through vegetation layer (path-1): σ_v
2. Double bounce scattering (path-2 and path-3): σ_{db}
3. Ground surface scattering (path-4): σ_g

The overall backscatter can be represented as an incoherent sum of individual contributions from these different scattering paths as:

$$\sigma = \sigma_v + \tau^2 \sigma_g + \sigma_{db} \tag{3.1}$$

where τ^2 represents the attenuation of the radar wave due to propagation through the vegetation layer (Ishimaru, 1978).

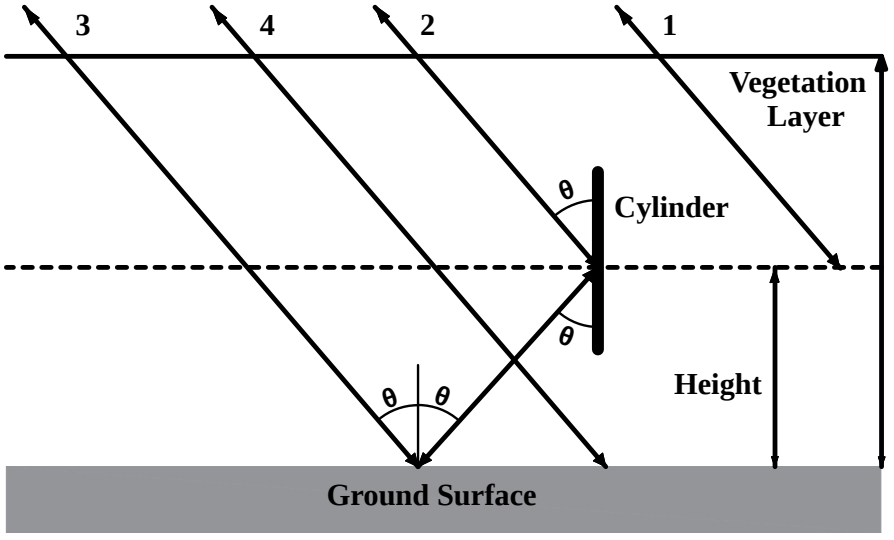

Figure 3.2: Different scattering mechanisms for a single layer vegetation model

3.2 Scattering from Vegetation Layer

The incident ray undergoes attenuation through the vegetation layer which is defined by

$$\begin{pmatrix} E_h \\ E_v \end{pmatrix}^{isc} = \begin{pmatrix} e^{-\tau_h(b-z)} & 0 \\ 0 & e^{-\tau_v(b-z)} \end{pmatrix} \begin{pmatrix} E_h \\ E_v \end{pmatrix}^{inc} = [\boldsymbol{\alpha}(b-z)] \begin{pmatrix} E_h \\ E_v \end{pmatrix}^{inc} \tag{3.2}$$

where E_h, E_v are the horizontally and vertically polarized electric fields. The superscripts isc and inc refers to the incident wave and scattered wave respectively. $\boldsymbol{\alpha}$ is the attenuation matrix given by:

$$\boldsymbol{\alpha} = \begin{pmatrix} e^{-\tau_h(b-z)} & 0 \\ 0 & e^{-\tau_v(b-z)} \end{pmatrix} \tag{3.3}$$

The incident wave first undergoes scattering and then it propagates through the vegetation layer with attenuation and returns to the radar. The scattered electric field for both polarization is given by the scattering matrix as follows:

$$\mathbf{S}_{veg}(\theta_i, \phi_i, \theta_s, \phi_s, \theta_c, \phi_c, z) = [\alpha(b-z)]\mathbf{S}(\theta_i, \phi_i, \theta_s, \phi_s, \theta_c, \phi_c)[\alpha(b-z)] \tag{3.4}$$

The radar cross-section can be derived from the elements of the covariance matrix which are defined as (Arii, 2009)

$$\begin{aligned} \boldsymbol{\Sigma}_{veg}(\theta_i, \phi_i, \theta_s = \theta_i, \phi_s = \phi_i, \theta_c, \phi_c, z) &= \begin{pmatrix} S_{HH} \\ \sqrt{2}S_{HV} \\ S_{VV} \end{pmatrix}_{veg} \left(S_{HH}\ \sqrt{2}S_{HV}\ S_{VV} \right)^*_{veg} \\ &= \begin{pmatrix} S_{HH}S_{HH}* & \sqrt{2}S_{HV}S_{HV}* & S_{HH}S_{VV}* \\ \sqrt{2}S_{HV}S_{HH}* & 2S_{HV}S_{HV}* & \sqrt{2}S_{HV}S_{VV}* \\ S_{VV}S_{HH}* & \sqrt{2}S_{VV}S_{HV}* & S_{VV}S_{VV}* \end{pmatrix}_{veg} \end{aligned} \tag{3.5}$$

We describe the density of vegetation through a function $\rho_s(z)$, which defines the scatterer density at a height z above the ground. To find the overall contribution from the

vegetation layer, we integrate the covariance matrix with respect to height as follows:

$$\langle \boldsymbol{\Sigma}_{veg}(\theta_i, \phi_i) \rangle = \int_0^b \langle \boldsymbol{\Sigma}_{veg}(\theta_i, \phi_i, z) \rangle \, \rho_s(z) \, dz \tag{3.6}$$

where $\langle \boldsymbol{\Sigma}_{veg}(\theta_i, \phi_i, z) \rangle$ is the ensemble average of $\boldsymbol{\Sigma}_{veg}(\theta_i, \phi_i, \theta_c, \phi_c, z)$ over all possible orientations of cylinder θ_c, ϕ_c.

$$\langle \boldsymbol{\Sigma}_{veg}(\theta_i, \phi_i, z) \rangle = \int_0^{2\pi} \int_0^{\pi} \boldsymbol{\Sigma}_{veg}(\theta_i, \phi_i, \theta_c, \phi_c, z) \, p(\theta, \phi) \sin\theta \, d\theta \, d\phi \tag{3.7}$$

Finally, the expression for the radar cross-section can be calculated as (van Zyl, 2011)

$$\boxed{\boldsymbol{\sigma}_{veg} = 4\pi \, \langle \boldsymbol{\Sigma}_{veg}(\theta_i, \phi_i) \rangle} \tag{3.8}$$

where where $\langle \boldsymbol{\Sigma}_{veg}(\theta_i, \phi_i) \rangle$ is the ensemble average of $\boldsymbol{\Sigma}_{veg}(\theta_i, \phi_i, \theta_c, \phi_c)$ over all possible orientations of cylinder θ_c, ϕ_c.

3.3 Backscatter from Underlying Ground Surface

The direct backscatter wave from the ground encounters vegetation in its path and hence the radar wave is attenuated due to dielectric effects of vegetation. The final scattered field that goes back to the radar can then be written in terms of the electric field scattered by ground as follows (Arii, 2009)

$$\begin{pmatrix} E_h \\ E_v \end{pmatrix}^{sc} = \begin{pmatrix} e^{-\tau_{hm}/\cos\theta_i} & 0 \\ 0 & e^{-\tau_{vm}/\cos\theta_i} \end{pmatrix} \begin{pmatrix} E_h \\ E_v \end{pmatrix}^{gr} \tag{3.9}$$

where the superscripts sc refer to the final backscattered field and gr refer to the field scattered by the ground before the attenuation.

In the same way, we can express the ground backscattering coefficients by multiplying the bare soil backscatter (calculated using I^{2}EM) with the attenuation factor as given below

$$\sigma^g_{HH} = e^{-2\tau_{hm}/\cos\theta_i} \sigma^{I^2EM}_{HH}(h, l, \epsilon_g) \tag{3.10}$$

$$\sigma_{VV}^{g} = e^{-2\tau_{vm}/\cos\theta_i}\sigma_{VV}^{IEM}(h, l, \epsilon_g) \tag{3.11}$$

where ϵ_g is the permittivity of soil and τ is the attenuation coefficient which depends upon vegetation characteristics. $\sigma_{HH}^{I^2EM}$ and $\sigma_{VV}^{I^2EM}$ are the backscatter coefficients calculated using Improved Integral Equation Model (Fung *et al.*, 2002).

3.4 Double Reflection Scattering

The double reflection scattering involves double reflection from the vegetation to the ground surface and back to the radar and vice-versa. For this, we consider bistatic scattering at the scatterer and specular scattering at the ground surface.

For the ground, the bistatic scattering matrix describing specular reflection is given by

$$\mathbf{R}_g(\theta_i, \phi_i, \theta_s, \phi_s) = \begin{pmatrix} R_h(\epsilon_g, \theta_i) & 0 \\ 0 & R_h(\epsilon_g, \theta_i) \end{pmatrix} e^{-2k^2h^2/\cos^2\theta_i} \tag{3.12}$$

where k is the wave number of the incident wave, h is the rms surface height, ϵ_g is the permittivity of soil and R_h and R_v are the Fresnel Reflection coefficients.

The total scattering matrix $\mathbf{S_{gc2}}$ for the path where the incident wave first undergoes specular scattering at the ground, followed by bistatic scattering at the cylinder is given by

$$\mathbf{S}_{gc2} = [\boldsymbol{\alpha}(b-z)] \begin{pmatrix} S_{HH} & S_{HV} \\ S_{VH} & S_{VV} \end{pmatrix} [\boldsymbol{\alpha}(z)] \begin{pmatrix} -1 & 0 \\ 0 & 1 \end{pmatrix} [\mathbf{R}_g][\boldsymbol{\alpha}(b)] \tag{3.13}$$

where S_{HH}, S_{HV}, S_{VH}, S_{VV} are the scattering coefficients for a single cylinder. Similarly, $\mathbf{S_{gc3}}$ represents the total scattering matrix for the path where the incident wave first undergoes bistatic scattering at the cylinder, followed by specular scattering at the ground.

$$\mathbf{S}_{gc3} = [\boldsymbol{\alpha}(b)]\,[R_g]\,[\boldsymbol{\alpha}(z)] \begin{pmatrix} -1 & 0 \\ 0 & 1 \end{pmatrix} \begin{pmatrix} S_{HH} & S_{HV} \\ S_{VH} & S_{VV} \end{pmatrix} [\boldsymbol{\alpha}(b-z)] \tag{3.14}$$

We now convert the scattering coefficients from the local coordinates relative to

cylinder orientation to the global coordinate system by the following matrix multiplication (van Zyl, 2011)

$$\begin{pmatrix} S_{HH} & S_{HV} \\ S_{VH} & S_{VV} \end{pmatrix} = \begin{pmatrix} \mathbf{h}_s \cdot \mathbf{h}'_s & -\mathbf{v}_s \cdot \mathbf{h}'_s \\ \mathbf{v}_s \cdot \mathbf{h}'_s & \mathbf{h}_s \cdot \mathbf{h}'_s \end{pmatrix} \begin{pmatrix} S_{HH} & S_{HV} \\ S_{VH} & S_{VV} \end{pmatrix} \begin{pmatrix} \mathbf{h}_i \cdot \mathbf{h}'_i & \mathbf{v}_i \cdot \mathbf{h}'_i \\ -\mathbf{v}_i \cdot \mathbf{h}'_i & \mathbf{h}_i \cdot \mathbf{h}'_i \end{pmatrix} \tag{3.15}$$

where h_i, v_i, h'_i, v'_i, h_s, v_s, h'_s, v'_s are the unit vectors in the global backscattering alignment system shown in Figure A.1.

The two signals propagating along the paths add coherently and thus the total scattering matrix S_{db} is given by

$$\mathbf{S}_{db} = \mathbf{S}_{gc2} + \mathbf{S}_{cg3} \tag{3.16}$$

The covariance matrix for the double reflection scattering is given by

$$\begin{aligned} \mathbf{\Sigma}_{veg}(\theta_i, \phi_i, \theta_s = \theta_i, \phi_s = \phi_i, \theta_c, \phi_c, z) &= \begin{pmatrix} S_{HH} \\ \sqrt{2} S_{HV} \\ S_{VV} \end{pmatrix}_{db} \left(S_{HH} \; \sqrt{2} S_{HV} \; S_{VV} \right)^*_{db} \\ &= \begin{pmatrix} S_{HH} S_{HH}* & \sqrt{2} S_{HV} S_{HV}* & S_{HH} S_{VV}* \\ \sqrt{2} S_{HV} S_{HH}* & 2 S_{HV} S_{HV}* & \sqrt{2} S_{HV} S_{VV}* \\ S_{VV} S_{HH}* & \sqrt{2} S_{VV} S_{HV}* & S_{VV} S_{VV}* \end{pmatrix}_{db} \end{aligned} \tag{3.17}$$

$$\langle \mathbf{\Sigma}_{veg}(\theta_i, \phi_i) \rangle = \int_0^b \langle \mathbf{\Sigma}_{veg}(\theta_i, \phi_i, z) \rangle \, \rho_s(z) \, dz$$

The radar cross section is calculated by taking the ensemble average of the components of the covariance matrix.

$$\boxed{\boldsymbol{\sigma}_{db} = 4\pi \, \langle \mathbf{\Sigma}_{db}(\theta_i, \phi_i) \rangle} \tag{3.18}$$

3.5 Simulation Results

Using Eq. 3.1, we calculate the total backscatter from vegetated lands as the sum of individual contributions from each path. To illustrate the effect of different vegetation parameters on the backscatter, we use the simulation parameters specified in Table 3.1 as input to our forward model. The simulation parameters has been chosen to simulate the backscattering from an agricultural land where the typical values of crop height and radius is around $50cm$ and $2mm$ respectively.

S.No.	Parameter	Value
1.	Cylinder radius (a)	2 mm
2.	Cylinder length (lc)	50 cm
3.	Cylinder density (ρ)	900 cylinders/m^3
4.	Vegetation layer height (b)	50 cm
5.	Orientation PDF $p(\theta_c, \phi_c)$	$\cos^2\theta_c \cos^2\phi_c$
6.	Surface rms height (h)	1 cm
7.	Surface correlation length (l)	15.2 cm
8.	Radar wavelength (λ)	24 cm
9.	Cylinder Dielectric Constant (vm)	13+5j
10.	Soil Moisture Content (mv)	0.3

Table 3.1: Parameters used in simulating the backscatter from a vegetation layer

3.5.1 Effect of Cylinder Radius

Different types of vegetation have different radar signatures which are a function of its height as well as radius. For example, a plant which has a thick stem of about $20\,mm$ radius (e.g. Guava tree) will have different radar backscatter as compared to a plant with thinner stalk with $3\,mm$ (e.g. maize). In this section, we will demonstrate the effect of changing cylinder radius on the vegetation backscatter as well as the extinction coefficient. The definition and details of calculating the extinction coefficient is given in Section A.4 of the Appendix.

From Figure 3.3, we observe that the extinction coefficient for both horizontal and vertical polarization increases with cylinder radius. This is due to the fact that there is

more attenuation due to thicker cylinders in case of vegetated lands. As the cylinder radius increases, the contribution of vegetation scattering increases as larger cylinders scatter more (Figure 3.4).

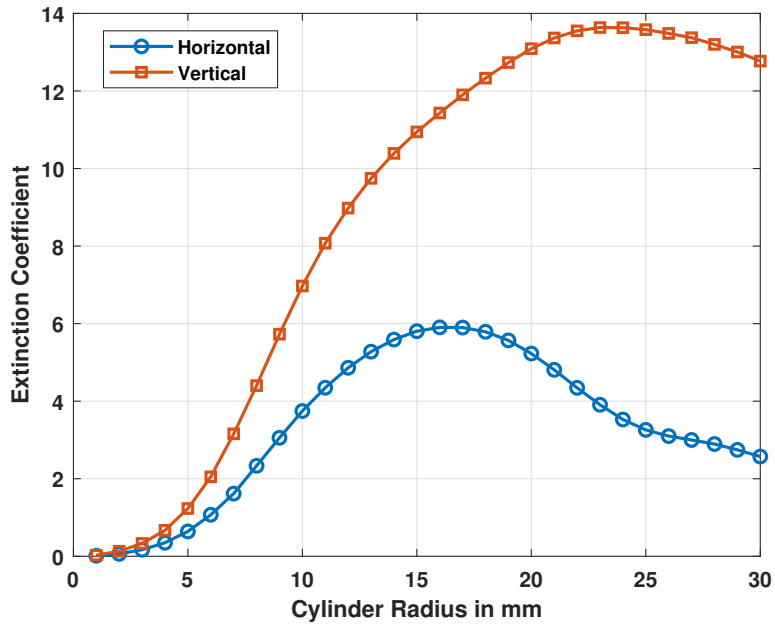

Figure 3.3: Extinction as a function of cylinder radius

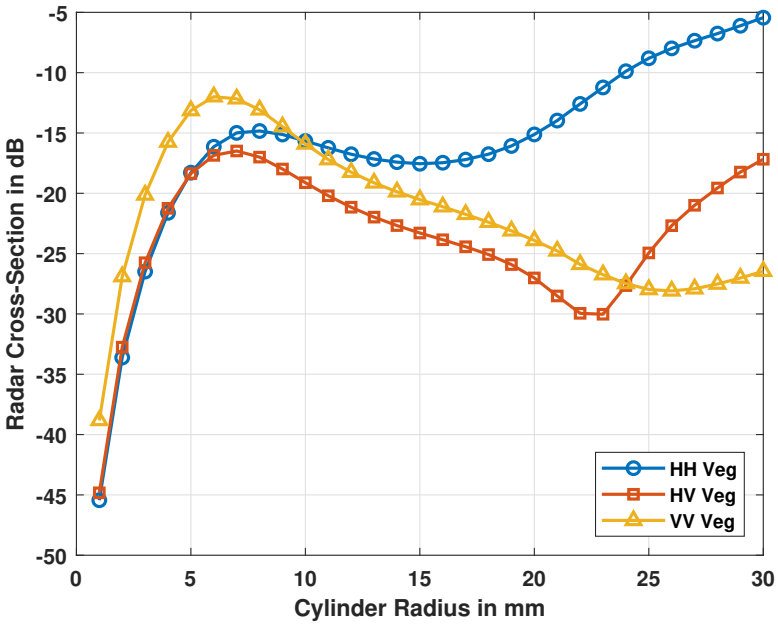

Figure 3.4: Scattering from vegetation layer as a function of cylinder radius

Figure 3.5 shows the scattering contribution of double bounce, ground backscatter and vegetation backscatter for HH polarization as a function of cylinder radius. We

observe that the surface scattering is more for thin cylinders whereas the double bounce scattering dominates for the thicker cylinder. For thicker cylinders, the contribution of ground backscatter is less sue to the attenuation of the ground wave from vegetation.

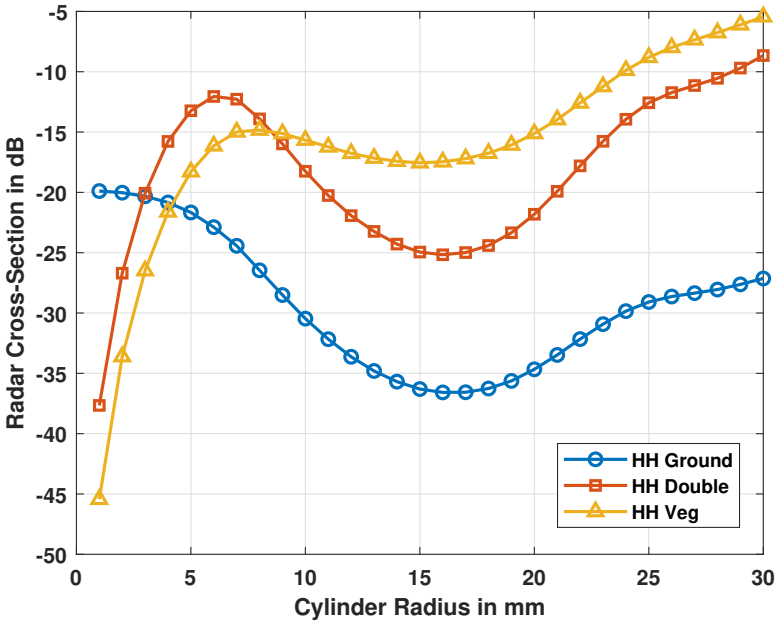

Figure 3.5: Scattering contributions of the different scattering mechanisms as a function of cylinder radius

3.5.2 Effect of the Angle of Incidence

The incidence angle of wave emitted by the radar determines the extent to total power comes back to radar after scattering from the vegetation as well as the underlying ground surface. A radar wave at low incident angle may not get backscattered significantly as it grazes the ground surface and doesn't get scattered back to the radar direction. Figure 3.6 shows the variation of backscattering coefficient as a function of incidence angle for HH polarization. From the figure, we can infer that the ground backscatter is dominant for low incidence angles for HH polarization. As the incidence angle increases, the double bounce and the vegetation backscatter starts to dominate.

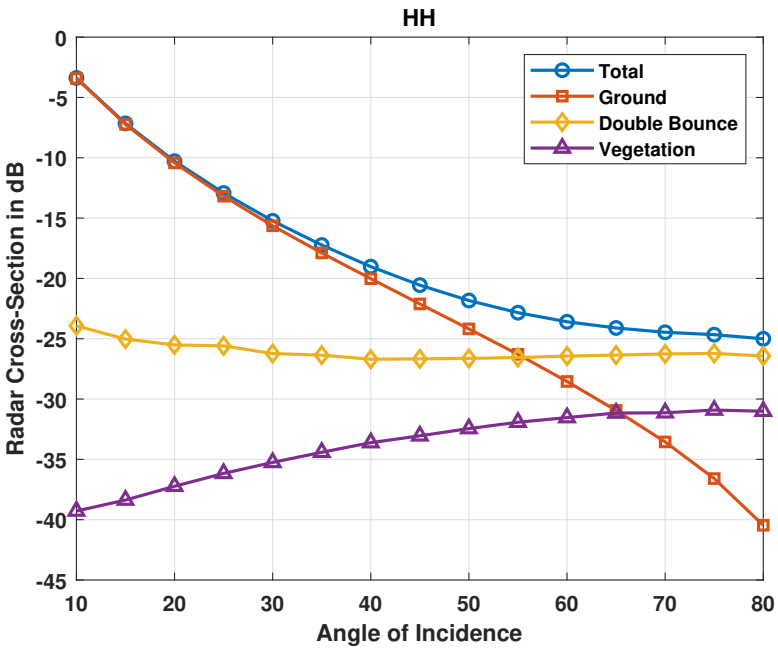

Figure 3.6: Backscatter cross sections as a function of angle of incidence at HH polarization

Figure 3.7 shows the variation of backscattering coefficient as a function of incidence angle for HV. In this cross-polarized backscatter, the contribution due to vegetation backscatter on total backscatter is high for low incidence angle. As the incidence angle increases, double bounce contribution increases due to more amount of scattering involved in that mechanism.

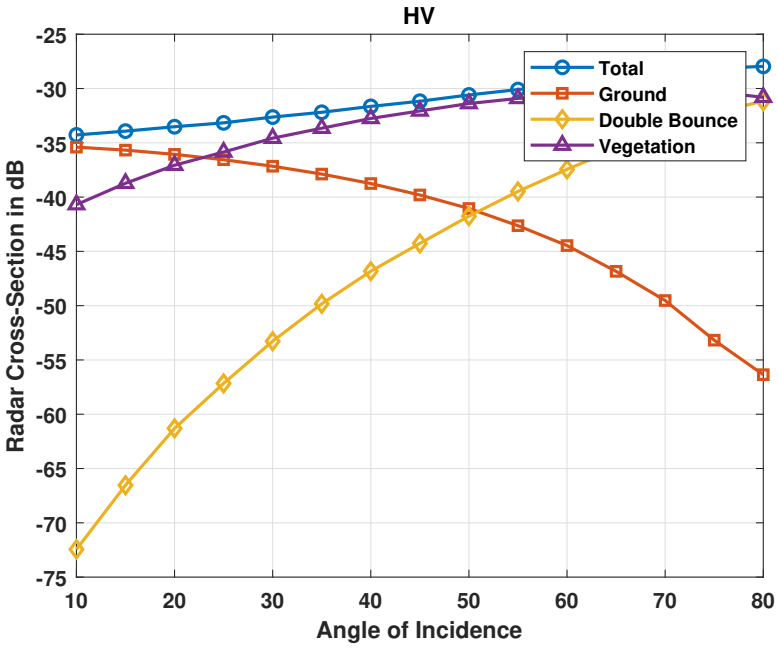

Figure 3.7: Backscatter cross sections as a function of angle of incidence at HV polarization

In case of VV polarization, the effects of incidence angle on backscatter is different as compared to other polarization. From Figure 3.8, we can see that the contribution of double bounce is very less to the overall backscatter as its magnitude is much lower as compared to the ground backscatter and the vegetation backscatter. We also observe that the ground backscatter dominates for all angle even if the effect of vegetation scattering increases slowly. This is because the vertical polarization VV doesn't interact with the upright cylinders which are the stems and stalks in our model as it is completely absorbed by them and much of the contribution comes from ground.

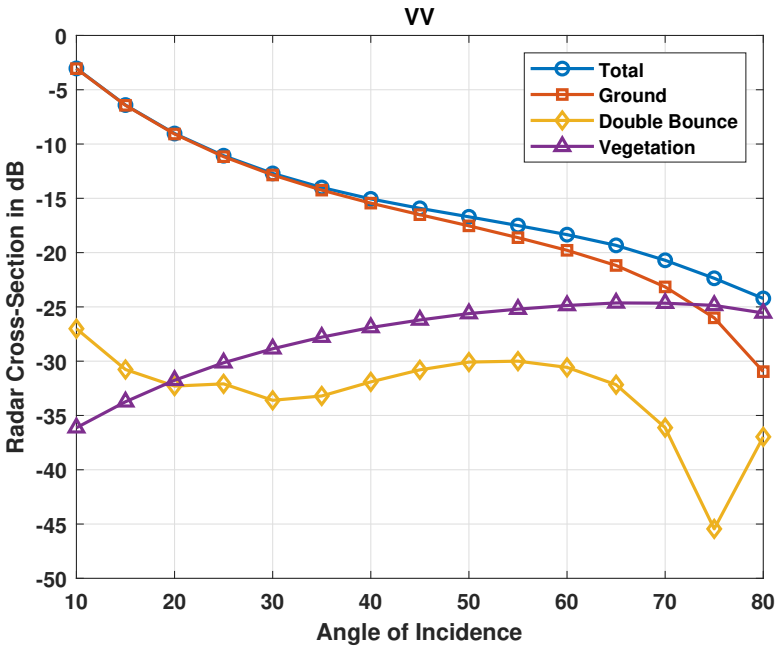

Figure 3.8: Backscatter cross sections as a function of angle of incidence at VV polarization

From the above figures, we saw that the scattering from vegetation depends on multiple parameters and that some form of scattering type dominates for a particular range of vegetation or radar parameters. For a typical radar incidence angle of 40^o, we can infer that double bounce reflection dominates at HH polarization, and vegetation scattering dominates for HV polarization while the ground backscatter is more dominant in case of VV polarization.

CHAPTER 4

SLICED REGRESSION INVERSION ALGORITHM

In this chapter, we will present the details of our inversion technique called the 'Sliced Regression Inversion Technique'. The algorithm can be divided into different modules and the functioning of each module is discussed separately as below:

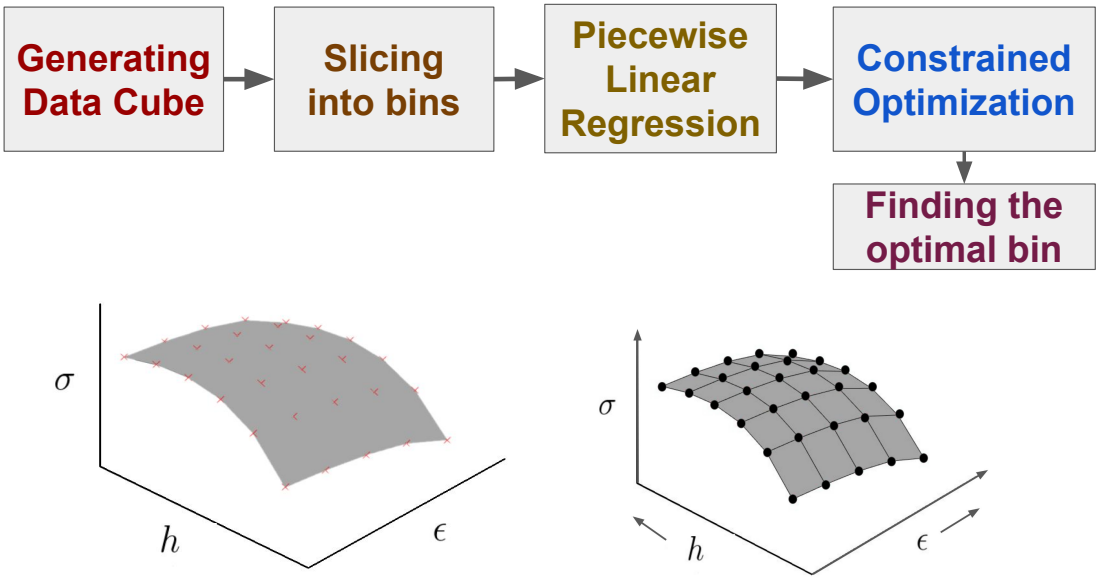

Figure 4.1: Block Diagram of Sliced Regression Inversion Algorithm

4.1 Data cube Generation

The first step in the SRI algorithm is to generate a data cube of backscatter coefficients for different combinations of soil and vegetation parameters. We use the Improved Integral Equation Model (I^2EM) to generate the ground backscatter and the dielectric cylinder approach (discussed in Chapter 3) as our forward scattering models to calculate the vegetation backscatter and the double bounce reflection. We then sum up the individual contributions from these scattering mechanisms to calculate the total backscatter.

The input parameters for a data cube are soil roughness rms surface height h, soil correlation length l, soil moisture mv and vegetation moisture vm, cylinder/vegetation

height l_{veg} and the cylinder radius a. The parameters - cylinder height and radius can be kept constant or can be taken as a parameter to be retrieved depending on the type of data-set and retrieval requirements. Each parameter is taken as an axis for the data cube with unit step along each axis taken as the difference between the adjacent values of that parameter. Thus any $d+1$-dimensional data cube consists of will have d independent parameter each representing one particular axis and one dependent variable which is the backscatter coefficient.

Each data cube has a unique set of radar parameters i.e. frequency f, incidence angle θ_i and the transmit-receive polarization pq which is unique to each data cube. By varying one or the other parameter, we can generate an entirely different data cube for the same set of soil and vegetation parameters. For example, in case of NISAR mission which has a SAR for L ($1.25\,GHz$) and S ($3\,GHz$) bands (Rosen *et al.*, 2017) and for HH, HV, and VV polarizations, we can have six different data cubes for these combinations: σ^L_{HH}, σ^L_{HV}, σ^L_{VV}, σ^S_{HH}, σ^S_{HV}, and σ^S_{VV} as show in Figure 4.2.

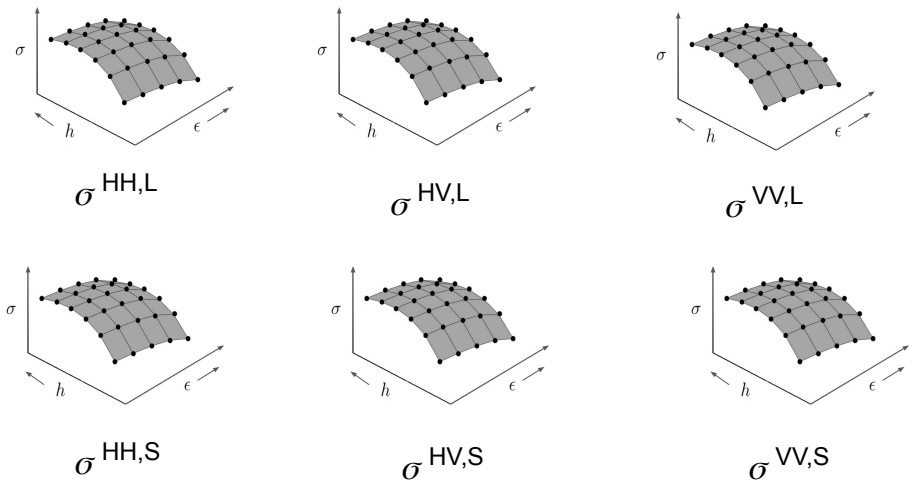

Figure 4.2: Illustration of six data cubes for each frequency and polarization combination

Mathematically, the backscattering coefficient for a radar operating at frequency f with polarization pq can be written as

$$\sigma^{pq,f} = F(h_i, l_i, m_{v_i}, v_{m_i}, pq, f) \,\forall\, i \in \{1, n\} \tag{4.1}$$

where F is the forward model, n is the total number of points in the data cube, f is the frequency and pq is the transmit-receive polarization which can be HH, HV or VV. The next step is the slicing of data cube into bins which is contructed between adjacent points of the data cube. For example, each bin of a datacube in $d+1$ dimensional space will have 2^d points. A graphical representation of a 2-dimensional data cube is given in Fig. 4.3.

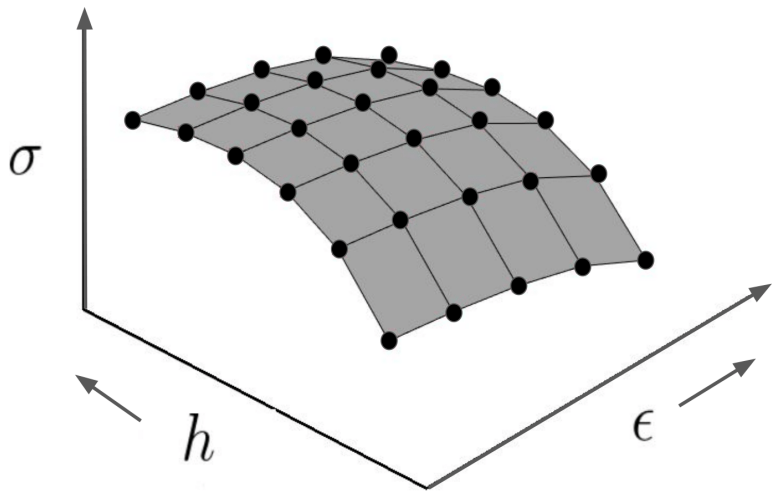

Figure 4.3: A graphical representation of a 2-dimensional datacube, with radar backscatter σ on the vertical axis and two input physical parameters h, ϵ on the horizontal axes. The circles represent the points computed by the forward model to populate the datacube. A piecewise linear model has been fit within each slice.

4.2 Piece-wise Linear Regression

Once the data cube is divided into bins, a linear relation is fit between the input and the output variables within each bin to generate a set of regression coefficients for each frequency-polarization combination. Within an arbitrary bin j, the backscatter $\sigma_{pq,f}$ can be expressed as the linear combination of the parameters in terms of regression coefficients $\beta_{pq,f}$ as follows:

$$\sigma^{pq,f} = \beta_{0,j}^{pq,f} + \sum_{i=1}^{d} \beta_{i,j}^{pq,f} v_i \tag{4.2}$$

where v_i is the i^{th} parameter belonging to bin j.

If the parameters to be retrieved are h, l, mv, and vm, the matrix equation for finding the the regression coefficients for each polarization frequency combination can be written as:

$$\underbrace{\begin{pmatrix} \sigma_1^{HH,L} & \sigma_1^{VV,L} & \sigma_1^{HH,S} & \sigma_1^{VV,S} & \sigma_1^{HV,L} & \sigma_1^{HV,S} \\ \sigma_2^{HH,L} & \sigma_2^{VV,L} & \sigma_2^{HH,S} & \sigma_2^{VV,S} & \sigma_2^{HV,L} & \sigma_2^{HV,S} \\ \vdots & \vdots & \vdots & \vdots & \vdots & \vdots \\ \sigma_n^{HH,L} & \sigma_n^{VV,L} & \sigma_n^{HH,S} & \sigma_n^{VV,S} & \sigma_n^{HV,L} & \sigma_n^{HV,S} \end{pmatrix}}_{\mathbf{Y}}$$

$$= \underbrace{\begin{pmatrix} 1 & h_1 & l_1 & m_{v_1} & v_{m_1} \\ 1 & h_2 & l_2 & m_{v_2} & v_{m_2} \\ \vdots & \vdots & \vdots & \vdots & \vdots \\ 1 & h_n & l_n & m_{v_n} & v_{m_n} \end{pmatrix}}_{\mathbf{X}} \underbrace{\begin{pmatrix} \beta_0^{HH,L} & \beta_0^{VV,L} & \cdots & \beta_0^{HV,S} \\ \beta_1^{HH,L} & \beta_1^{VV,L} & \cdots & \beta_1^{HV,S} \\ \vdots & \vdots & \ddots & \vdots \\ \beta_4^{HH,L} & \cdots & \cdots & \beta_4^{HV,S} \end{pmatrix}}_{\boldsymbol{\beta}} \tag{4.3}$$

where $n = 32$ is the number of points within each bin since the dimension $d = 5$ in this case.

However, Eq. 4.2 has infinitely many solutions as it is a rectangular matrix and hence not full rank. So we solve the matrix equation using least squares principle, i.e.

$$\hat{\boldsymbol{\beta}} = \underset{\boldsymbol{\beta}}{\text{argmin}} \|\mathbf{X}\boldsymbol{\beta} - \mathbf{Y}\|^2 = (\mathbf{X}^T\mathbf{X})^{-1}\mathbf{X}^T\mathbf{Y} \tag{4.4}$$

4.3 Soil moisture retrieval

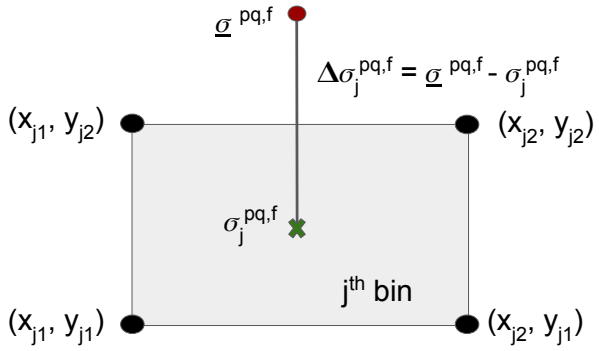

Figure 4.4: Projecting a data point onto a 2D plane

After getting the regression coefficients for each bin, we proceed to estimating the soil moisture given the radar data. We find the bin which gives the least error from the knowledge of regression coefficients. We project the given data point onto the hyper-plane constructed within each bin as shown in Fig. 4.4 and find the residual error for that bin $\sigma_{true} - \sigma_{projected}$. Taking the norm of the residual error from all combinations of frequency and polarization, we get the overall error for that particular bin. We solve a bounded least squares equation to find the bin k which gives the lowest residual error as follows:

$$k = \underset{j}{\operatorname{argmin}} \left\{ \sum_{pq,f} \|\bar{\sigma}^{pq,f} - \sigma^{pq,f}(\vec{x})\|^2 \text{ s.t. } \vec{x} \in \mathcal{B} \right\} \tag{4.5}$$

This equation can be written in the matrix form as follows

$$\underbrace{\begin{pmatrix} \sigma_k^{HH,L} - \beta_{0,k}^{HH,L} \\ \sigma_k^{VV,L} - \beta_{0,k}^{VV,L} \\ \sigma_k^{HV,L} - \beta_{0,k}^{HV,L} \\ \sigma_k^{HH,S} - \beta_{0,k}^{HH,S} \\ \sigma_k^{VV,S} - \beta_{0,k}^{VV,S} \\ \sigma_k^{HV,S} - \beta_{0,k}^{HV,S} \end{pmatrix}}_{\vec{z}} = \underbrace{\begin{pmatrix} \beta_{1,k}^{HH,L} & \dots & \beta_{d,k}^{HH,L} \\ \beta_{1,k}^{VV,L} & \dots & \beta_{d,k}^{VV,L} \\ \beta_{1,k}^{HV,L} & \dots & \beta_{d,k}^{HV,L} \\ \beta_{1,k}^{HH,S} & \dots & \beta_{d,k}^{HH,S} \\ \beta_{1,k}^{VV,S} & \dots & \beta_{d,k}^{VV,S} \\ \beta_{1,k}^{HV,S} & \dots & \beta_{d,k}^{HV,S} \end{pmatrix}}_{\boldsymbol{\beta}} \underbrace{\begin{pmatrix} x_1 \\ \vdots \\ x_d \end{pmatrix}}_{\vec{x}} \tag{4.6}$$

Once we find the optimal bin k, the next step is to retrieve the physical parameters, $\vec{x}$. For that, we substitute the measured backscatter values $\bar{\sigma}^{pq,f}$ on the left hand side of Eqn. 4.6 to get the vector $\vec{y}$ as follows:

$$y_i = \bar{\sigma}^{pq,f} - \beta_{0,k}^{pq,f} \tag{4.7}$$

However, due to measurement noise and modelling errors, the measured backscatter values $\vec{y}$ differ from the predicted backscatter values, i.e. $\vec{y} \neq \boldsymbol{\beta}\vec{x}$. Figure 4.4 shows how the measured backscatter point doesn't lie in the hyperplane constructed within the bin and thus we find the projection of that point in the plane which explains the data with the least error. So, we find $\vec{x}$, i.e. the physical parameters by solving the following bounded least squares equation in the bin k.

$$\hat{\vec{x}} = \underset{\vec{x}}{\text{argmin}} \|\vec{y} - \boldsymbol{\beta}\vec{x}\|^2 \; s.t. \; \vec{x} \in \mathcal{B}_k \tag{4.8}$$

At the end of this procedure, we have determined the entire set of physical parameters that best explain the radar backscatter, including soil moisture.

Note: Although the name matches, the sliced inversion regression (SIR) technique (Li, 1991)) from statistics used for dimension reduction is different from the proposed sliced regression inversion (SRI) technique to retrieve soil moisture in this thesis. The SIR technique from statistics uses concepts from multivariate and conditional probability for dimensionality reduction. On the other hand, the proposed SRI algorithm relies only on finding regression coefficients and solving the least squares equation to estimate unknown coefficients.

CHAPTER 5

RETRIEVAL RESULTS USING SRI ALGORITHM

In this chapter, we present the result and analysis of soil moisture retrieval using the Sliced Regression Inversion (SRI) algorithm. We apply our algorithm on real as well as synthetically generated test datasets and validate the estimated soil moisture with the ground truth data. In the synthetic case, we generate few random test points within the range of the data cube. To simulate a realistic scenario where there is measurement and radar noise involved, we add additive white Gaussian noise of 10 dB SNR added to the measurements. The noise N in dB scale) can be calculated from the signal to noise ratio (SNR) using the following relation:

$$N = 10\log_{10}(1 + 10^{(-\mathrm{SNR}/10)}) \tag{5.1}$$

Thus, an SNR of 10 dB corresponds to $N = 0.5\,dB$ perturbation in the backscatter values. To test the accuracy of our inversion model, we compare the retrieval results using the SRI algorithm with a widely employed semi-empirical model called the Soil Moisture Assessment Radar Technique (SMART) inversion algorithm (Dubois *et al.*, 1995) for the bare soil case. We also study the effect of adding dual-band information of backscatter coefficients and the subsequent improvement in the retrieval accuracy. We also discuss the case where the soil is considered to be heterogeneous in which the dielectric has a vertical gradient and thus the moisture varies with depth. Using ALOS-2 PALSAR and SENTINEL satellite data, we present the retrieval results in the presence of vegetation for three different cases - maize, chilli, and jowar.

5.1 Implementation Details

The SRI algorithm was implemented in MATLAB and executed on a 3.60GHz Intel Octa-Core i7 processor with 16 GB RAM. The alternating direction method of multipliers (ADMM) (Boyd *et al.*, 2011) is used to implement the bounded least squares

algorithm as per Eqs. 4.5,4.8, with the stopping criteria being that the relative change in the solution to either equation is less than 10^{-2}.

Parameter	Value
Incidence Angle	37^o
Sand texture	$34\,\%$
Clay texture	$25\,\%$
Cylinder radius	Variable
Cylinder length	Variable
Cylinder density	10 plants/m^2
Vegetation layer height	50 cm
Orientation PDF $p(\theta_c, \phi_c)$	$\cos^2\theta_c \cos^2\phi_c$

Table 5.1: Fixed parameter values for data cube generation

5.2 Comparison with SMART inversion algorithm

In this section, we show the retrieval accuracy of our algorithm in comparison with the Soil Moisture Assessment Radar Technique (SMART) (Dubois *et al.*, 1995), which is a semi-empirical soil moisture retrieval algorithm. SMART has been a very popular technique due to its simplistic nature and good retrieval accuracy. For the sake of comparison, we use the SMART forward model to generate the backscattering coefficients for populating the data cube for retrieval purposes.

According to the SMART forward model, the backscattering cross-section σ_{HH} and σ_{VV} are empirically determined as

$$\sigma_{HH} = 10^{-2.75}\frac{\cos^{1.5}\theta}{\cos\theta^5}10^{0.028\epsilon\tan\theta}(kh\sin^{1.4}\theta)\lambda^{0.7} \tag{5.2}$$

$$\sigma_{VV} = 10^{-2.35}\frac{\cos^{3}\theta}{\cos\theta}10^{0.046\epsilon\tan\theta}(kh\sin^{3}\theta)^{1.1}\lambda^{0.7} \tag{5.3}$$

The SRI and SMART inversion algorithm was applied on a synthetic data generated from taking random test data points using the SMART forward model with 0.6 dB noise

added. The computer codes for implementing SMART forward and inverse model were obtained from MRS-UMICH website (Ulaby, 2014). The estimated and actual values of soil moisture for both these algorithms are shown in Figure 5.1 and the results are tabulated in Table 5.2 along with the retrieval results for a wavelength of $\lambda = 24\,cm$ and incidence angle $\theta_i = 40^o$ are shown in Table 5.2. From the results tabulated below, it is evident that the Sliced Regression Inversion algorithm gives more accurate results than the SMART algorithm for the retrieval of soil moisture (mv) as well as rms height (h).

Algorithm	$\mathbf{h(cm)}$	$\mathbf{mv(cm^3/cm^3)}$
SRI	0.20	0.053
SMART	0.25	0.07

Table 5.2: Table of RMSE values for soil moisture retrieval using SMART and SRI algorithm

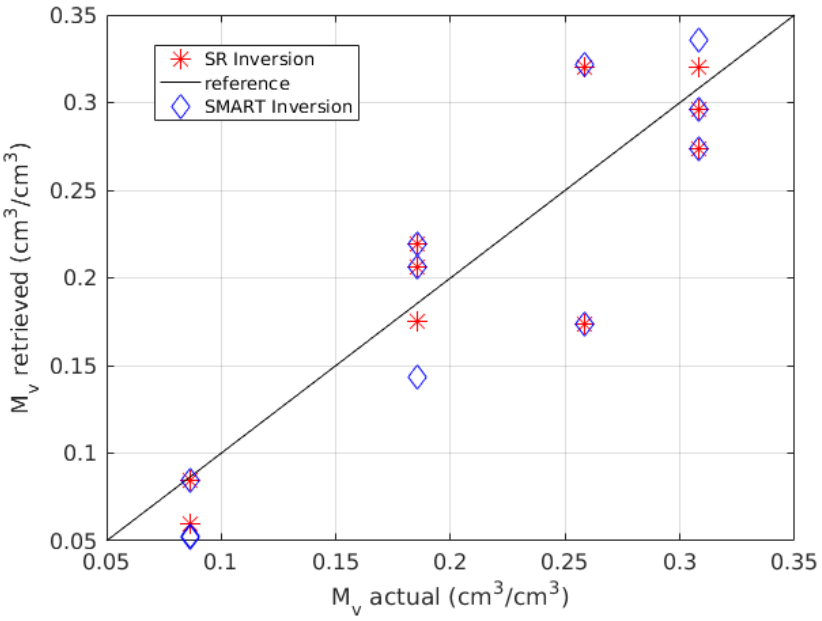

Figure 5.1: Comparison between SMART and proposed SRI algorithm

5.3 Bare soil with depth-dependent moisture

It is generally seen that soil dries from top-down after a spell of rain and develops a vertical dielectric gradient. Thus, the soil structure becomes highly heterogeneous and

soil moisture varies with depth. Due to this inhomogeneity of soil structure, there are challenges involved in the soil moisture retrieval process. So, we modify the Integral Equation Model (Fung *et al.*, 1992), which assumes the soil to be homogeneous, to incorporate an exponential dielectric profile (Fung *et al.*, 1996) and calculate the radar backscatter by modifying the reflection coefficient from the soil surface (Section 2.4).

Retrieval is done for a heterogeneous soil surface where the soil is assumed to have a vertical dielectric profile i.e. the soil moisture varies with depth. We use the co-polarized backscatter components σ_{HH} and σ_{VV} as our radar observations for retrieval purpose. The model assumes piecewise constant values of soil permittivity for depths of $0 - 0.1\,m$ in steps of $0.01\,m$. The retrieval accuracy ($\%$ error) for rms surface height h, correlation length l, soil permittivity ϵ, and transition rate factor m for both noiseless and $0.5\,dB$ noise is summarized in the Table 5.3. The ranges of parameter used for generating the data cube are mentioned in the table captions. We use synthetically generated test data for the retrieval process. We also show the corresponding retrieval for homogeneous soil profile for a comparison. For a general case of random test data with $0.5\,dB$ added noise, we get an RMSE of 0.08 for homogeneous soil profile and an RMSE of 0.03 for heterogeneous profile. Figure 5.2 shows the variation of retrieved value of soil permittivity with depth for both noiseless and $0.5\,dB$ case.

Soil Profile	**Homogeneous**		**Heterogeneous**	
Noise level	**h**	**mv**	**h**	**mv**
0 dB	0.11	0.04	0.25	0.03
0.5 dB	0.28	0.06	0.33	0.03

Table 5.3: Retrieval results (RMSE error) for depth dependent moisture with random test data using SRI algorithm. Range of data cube parameters: $h = [0.5 : 1 : 3.5]$, $l = [5 : 10 : 25]$, $mv = [0.05 : 0.09 : 0.55]$, , $m = [-6 : 6 : 6]$

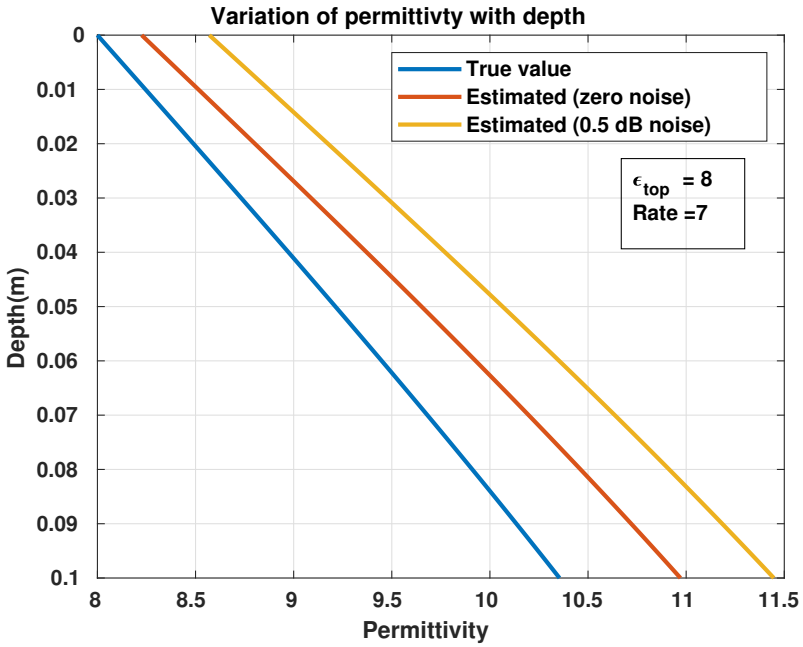

Figure 5.2: Variation of soil permittivity with depth. Range of data cube parameters: ($\epsilon_{top} = 8$) and transition rate factor ($m = 7$) Range: $h = [0.3, 0.7, 1.5]$, $l = [4, 18, 34]$, $\epsilon = [3, 7, 12, 19]$, , $m = [0, 4, 8, 12]$

5.4 NISAR Inversion results (Synthetic)

We test the accuracy of our inversion algorithm on the synthetic data generated for the NISAR operating bands (L and S) with three transmit-receive polarization combinations available (HH, HV, and VV). The parameters used to generate data cube are shown in Table 5.1. Similar to the above cases, we add a $0.5\,dB$ noise using an SNR of 10 dB. Table 5.4 presents the results for single versus dual-band retrieval for bare and vegetated lands in terms of the root mean squared error (RMSE) and the correlation coefficient (R2). All numbers are averaged over 10 instances of Monte Carlo iterations with zero-mean Gaussian noise of variance 0.5 dB in each iteration.

From the Table 5.4, we observe that using quad-polarized dual band backscatter data [HH+VV+HV]-L,S gives the best accuracy for both bare-soil and vegetated lands. Moving from single band to dual-band retrieval, the accuracy increases from 10% RMSE to 5% for bare soil and from 12% RMSE to 6% for vegetated lands.

In case of vegetated lands, it is generally found that adding cross-polarized information can lead to an increase in the root mean squared error in soil moisture (Kim

et al., 2013). This is because of the fact that the cross-polarised backscatter HV is more sensitive to the vegetation and hence prone to modelling errors as well as measurement noise. Modelling errors arise due to inability of the forward model I^{2}EM to capture multiple scattering events, which are significant in determining cross-polarized component of backscatter. These issues can be overcome by the use of more accurate forward models, e.g. Advanced Integral Equation Model (Yang *et al.*, 2017), (Yang and Chen, 2019). Since the test data used in generating these results were synthetic, modelling errors didn't arise and hence there was no decrease in accuracy after adding the cross-polarized component.

From the Table 5.4, we also observe that L-band retrievals using SRI algorithm yield better accuracy as compared to S-band retrievals. However, if we add more information, i.e. use dual band co-pol backscatter data for the retrieval process, the retrieval accuracy is increased.

Measurement	**Vegetated Land**		**Bare Soil**	
	RMSE	**R2**	**RMSE**	**R2**
[HH+HV]-L	0.11	0.44	0.14	0.14
[HH+HV]-S	0.12	0.36	0.12	0.28
[VV+VH]-L	0.08	0.70	0.10	0.47
[VV+VH]-S	0.11	0.45	0.12	0.29
[HH+HV]-[L,S]	0.07	0.76	0.07	0.71
[VV+VH]-[L,S]	0.10	0.51	0.08	0.63
[HH+VV]-[L,S]	0.09	0.66	0.07	0.71
[HH+VV+HV]-[L,S]	0.06	0.79	0.05	0.81

Table 5.4: Comparison of single and dual band soil moisture retrieval accuracy (RMSE in cm^3/cm^3) for SRI algorithm over vegetated and bare soils using synthetic data for different configurations of polarization/frequency; The fixed parameters of the data cube are as per Table 5.1, while the variable parameters are: surface roughness, $h = [0.5 : 0.7 : 4]$ cm, surface correlation length, $l = [5, 25]$ cm, soil moisture, $mv = [0.05 : 0.05 : 0.55]$ cm^3/cm^3, vegetation moisture, $vm = [0.05 : 0.1 : 0.55]$ cm^3/cm^3, vegetation length $l_{veg} = [50 : 100 : 250]$ cm, and vegetation radius $r_{veg} = [2 : 3 : 8]$ mm.

Measurement	Vegetated Land		Bare Soil	
	RMSE	R2	RMSE	R2
HH-L	0.13	0.28	0.16	0.05
VV-C	0.14	0.20	0.14	0.26
[HH+HV]-L	0.11	0.44	0.14	0.07
[VV+VH]-C	0.13	0.34	0.15	0.09
HH-L, VV-C	0.12	0.39	0.12	0.13
[HH+HV]-L, VV-C	0.09	0.63	0.12	0.33
[HH+HV]-L, [VV+VH]-C	0.13	0.33	0.13	0.23
[HH+VV+HV]-L,C	0.09	0.64	0.12	0.37

Table 5.5: Retrieval results using SRI for vegetated surface (synthetic) using L & C-band data; The data cube of 3240 points has the same specifications as in Table 5.4

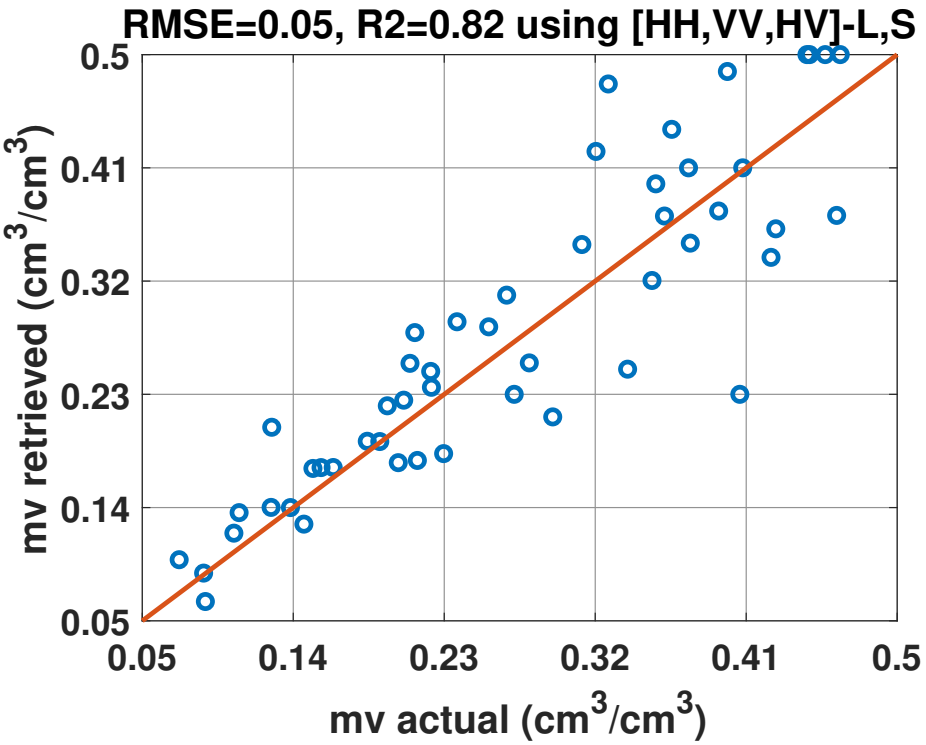

Figure 5.3: Scatter plot showing performance of SRI algorithm for soil moisture retrieval using dual (L+S) band (synthetic) data over bare soil

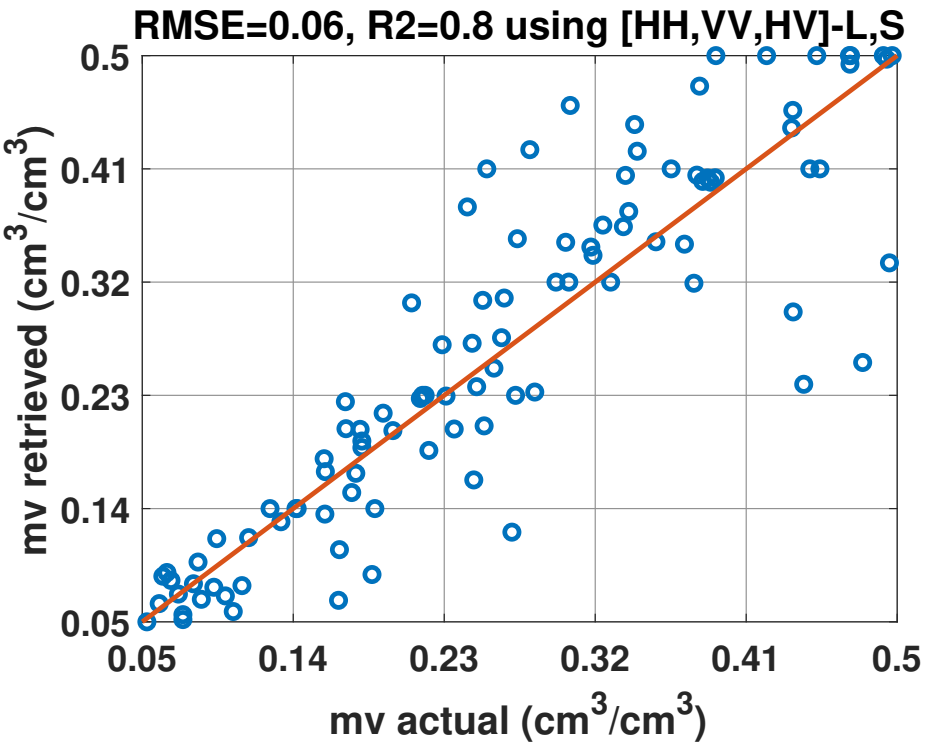

Figure 5.4: Scatter plot showing performance of SRI algorithm for soil moisture retrieval using dual (L+S) band (synthetic) data over vegetated soils

5.5 Inversion Results on Experimental Data

In this section, we test the retrieval accuracy of our SRI algorithm on experimental data. We use the backscatter information collected at L-band from the ALOS PALSAR sensor (HH and HV), and C-band from the SENTINEL-1A sensor (VV and VH) as the radar information. Details about the SAR datasets, selected test sites, and the collection of ground truth (GT) over these sites have been mentioned in Appendix B.

Measurement	Maize	Chilli	Jowar	Bare Soil
HH-L	0.20	0.16	0.19	0.16
VV-C	0.31	0.20	0.33	0.18
[HH,HV]-L	0.20	0.18	0.23	0.22
[VV,VH]-C	0.31	0.17	0.35	0.07
HH-L,VV-C	0.21	0.14	0.17	0.13
[HH,HV]-L,VV-C	0.20	0.23	0.24	0.16
[HH,HV]-L,VH-C	0.20	0.16	0.24	0.14
HH-L,[VV,VH]-C	0.21	0.18	0.25	0.06
HV-L,[VV,VH]-C	0.32	0.17	0.35	0.06
[HH,HV]-L,[VV,VH]-C	0.20	0.18	0.26	0.06

Table 5.6: SRI Retrieval results for ALOS-PALSAR (L-band) and SENTINEL-1A (C-band) dual band for maize, chilli, jowar crops and bare soil; Each row correspond to retrieval using different combinations of polarization-frequency measurement used. The data cube of 3240 points has the same specifications as in Table 5.4

In these simulations, both the vegetation layer height l_{veg} and vegetation radius r_{veg} is also taken as a parameter to be retrieved by adding it as another axis to the data cube. This is because the crop height and radius was not uniform during the fieldwork campaign (Figure B.1). Table 5.6 show the retrieval results (characterized by RMSE in mv) for bare soil and croplands (maize, chili, and jowar) for different combinations of frequency and polarization. Table 5.7 shows the retrieval results on synthetically generated test data sets for L and C bands for the same combinations of frequency and polarization. In Figures 5.5, 5.6, 5.7, and 5.8, we show scatter plots depicting the actual versus retrieved values of soil moisture for bare soil, maize, chilli and jowar covered lands respectively.

From Table 5.6, we observe that we get the best accuracy using the dual-band backscatter combination with both synthetic data (RMSE $= 0.09$ cm^3/cm^3) and experimental data (RMSE $= 0.06$ cm^3/cm^3) for bare soil. For vegetation-covered lands, the best retrieval accuracies for synthetic and experimental data are about $4-5\%$ different which can be due to modelling or data collection error. The best accuracy for maize crop is achieved by fixing the cylinder radius to be 5 mm and variable cylinder length. For chilli crop, the best accuracy is achieved at a fixed radius of 2 mm and cylinder

length of 50 cm. The lower values of soil moisture are retrieved with good accuracy of 0.06 cm^3/cm^3whereas for higher moisture values, the accuracy degrades. Retrieval using jowar crop is best explained with a fixed radius of 2mm and variable length.

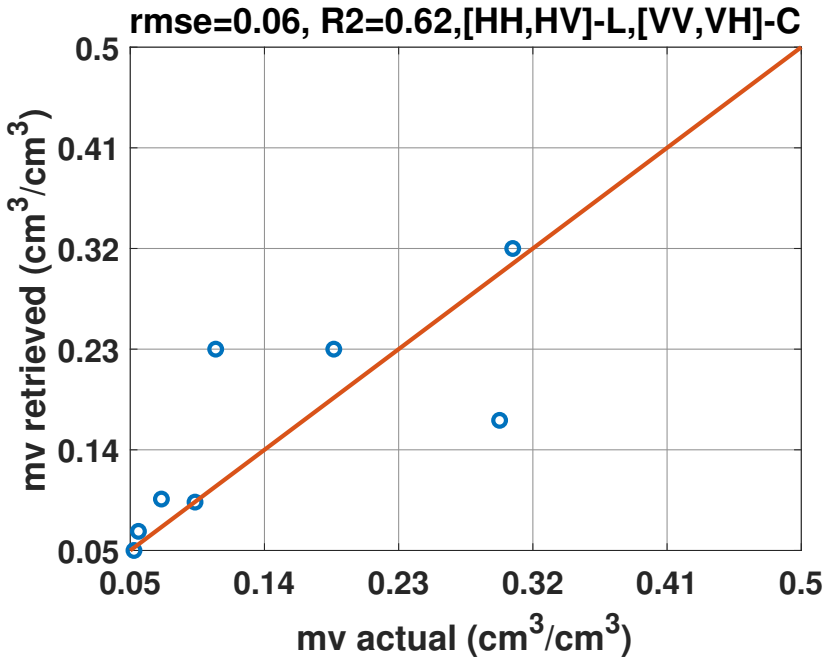

Figure 5.5: Retrieval accuracy of SRI approach for bare soil using the [HH,HV]-L, [VV,VH]-C component of the backscatter from the experimental data.

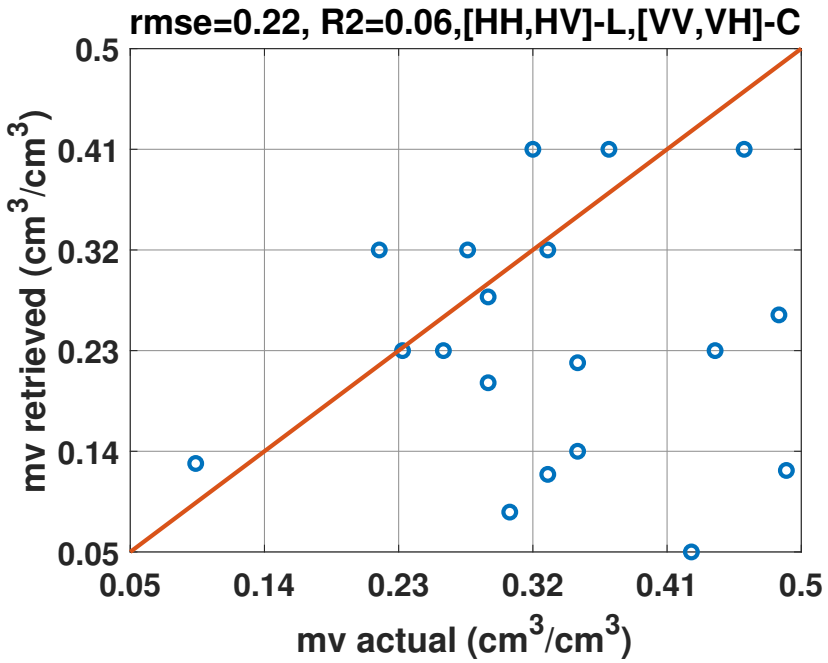

Figure 5.6: Retrieval accuracy of SRI approach for maize crop using the [HH,HV]-L, [VV,VH]-C component of the backscatter from the experimental data.The data cube parameters are as per the Table 5.5. except that the cylinder radius is fixed at 5mm. There must be either modelling error or an incorrect fixed parameter causing the mismatch.

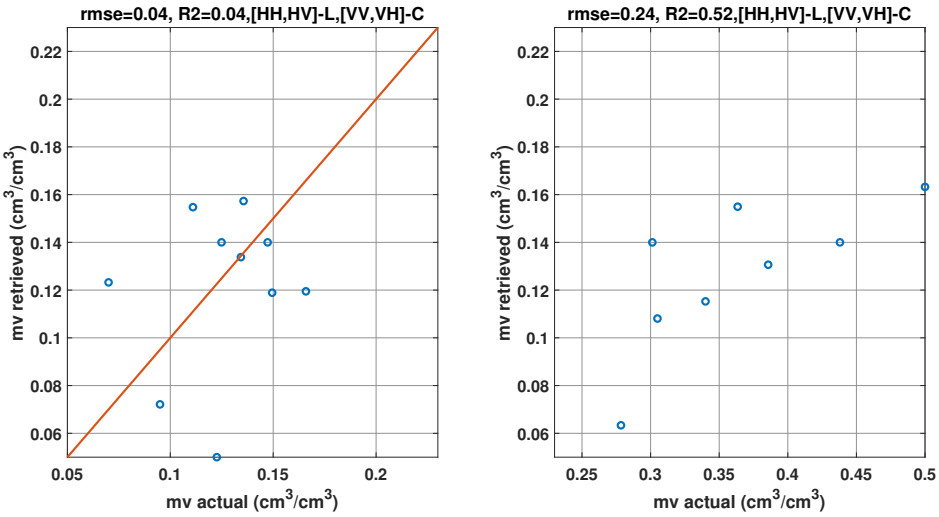

Figure 5.7: Retrieval accuracy of SRI approach for chilli crop using the [HH,HV]-L, [VV,VH]-C component of the backscatter from the experimental data.The data cube parameters are as per the Table 5.5. except that the cylinder radius and cylinder length are fixed at 2mm and 50 cm respectively.

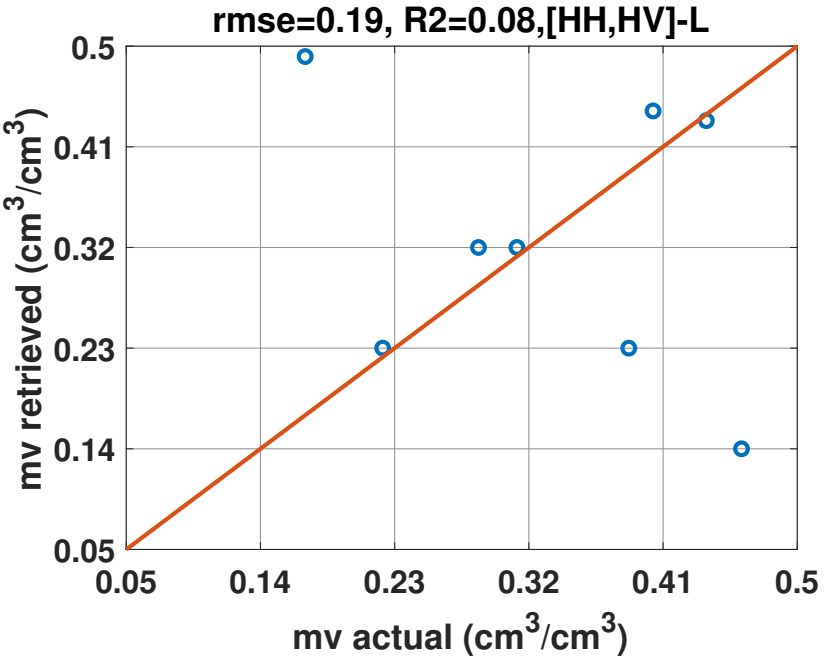

Figure 5.8: Retrieval accuracy of SRI approach for jowar crop using the [HH,HV]-L, [VV,VH]-C component of the backscatter from the experimental data.The data cube parameters are as per the Table 5.5. except that the cylinder radius is fixed at 2mm

5.6 Comparison with LUT-Approach

In this section, we show the comparison of the retrieval accuracy and time of our Sliced Regression Inversion algorithm with the lookup table approach (Kim *et al.*, 2011, 2013). The SRI algorithm gives a better estimate than LUT by projecting it onto the hyperplane constructed within the grid while the LUT finds the nearest grid point to the test data point. Thus, the LUT estimate is limited by the degree of fineness of the grid while it doesn't have much effect on SRI accuracy because of its ability to linearly approximate the relation between the backscatter and the input parameters. Table 5.7 shows the retrieval accuracy of both SRI and LUT applied on experimental and synthetic datasets for bare soil and for vegetated lands, i.e., maize, jowar and chilli crops with the ground truth data being used for calculating the RMSE errors in soil moisture.

Algorithm	**Maize**	**Chilli**	**Jowar**	**Bare Soil**
SRI	0.2	0.18	0.26	0.06
LUT	0.43	0.27	0.47	0.17

Table 5.7: Comparison of SRI and LUT algorithm for the vegetated land (maize, jowar and chilli) and bare soil using the ALOS-PALSAR (L-band) and SENTINEL-1A (C-band). The reported accuracy (RMSE) is using all the measurement available [HH,HV]-L,[VV,VH]-C. The data cube parameters are as per the Table 5.5.

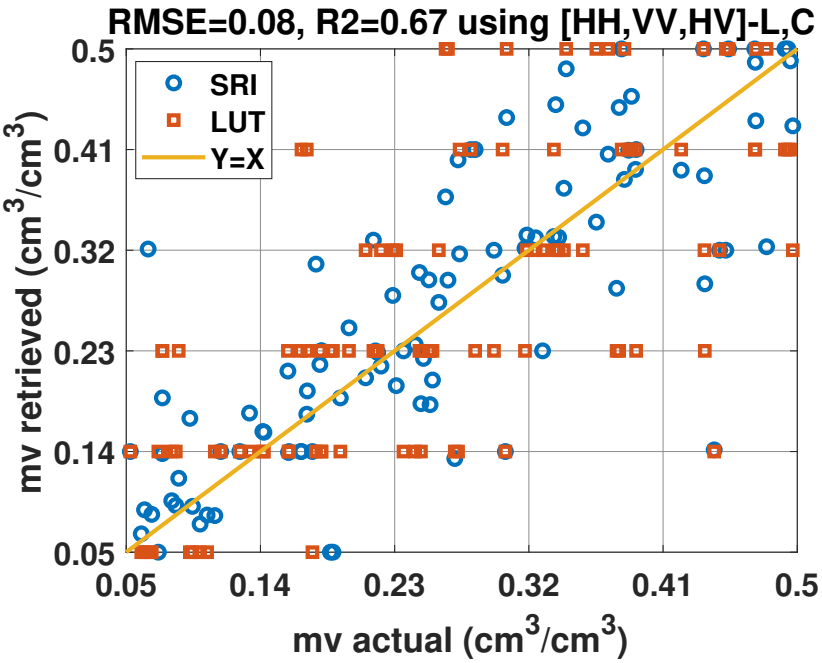

Figure 5.9: Comparison of retrieval accuracy of SRI with the look-up table (LUT) approach for synthetic data using the full-band data [HH,VV,HV]-L,C. The data cube parameters are as per the Table 5.5.

To find out the effect of varying fineness of the data cube on the retrieval accuracy, we perform both LUT and SRI algorithm on synthetic data using different grids and plot the resulting accuracies in Figure 5.10. From the figure, we observe that a data cube of size 1000 is required by the SRI algorithm to achieve an accuracy of < 0.10 cm^3/cm^3while the LUT approach requires a much finer and bigger data cube(Size: 2000) for the same accuracy.

Next, we analyse the data cube generation time as a function of size of data cube and compare the time taken for retrieval using the SRI and LUT approaches. Figure 5.11 shows both these plots with the left axis showing the retrieval time and the right axis showing the time taken to generate the data cube. We observe that LUT takes lesser time than SRI to retrieve soil moisture using a given size of data cube and this time scales linearly with data cube size for both these approaches.

Since the LUT approach requires a bigger and finer data cube than the SRI approach to get the same accuracy, the data cube generation time is also different for both approaches. For example, < 0.10 cm^3/cm^3accuracy is achieved when SRI uses a datacube of size 1000 which is prepared in 20 hours. The same accuracy is achieved by the LUT approach using a data cube prepared in 50 hours. So, the computation cost in-

volved with changing any of the input parameters (e.g. incidence angle, cylinder radius, etc.) is much greater with LUT approach as compared to the SRI approach. Thus, the SRI algorithm offers significant advantage over LUT approach both in case of retrieval accuracy and computational time.

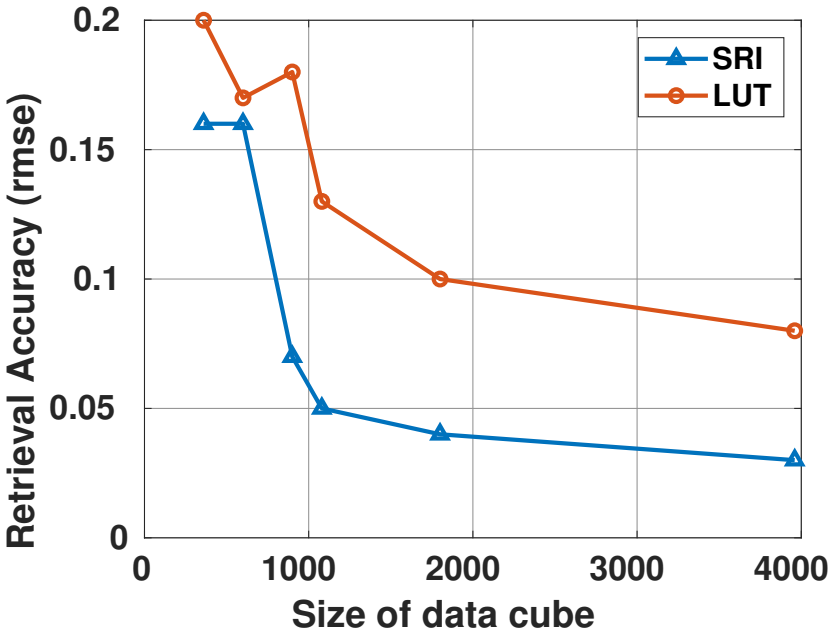

Figure 5.10: Comparison of retrieval accuracy of SRI and LUT approach for various sizes of data cube using synthetic data.

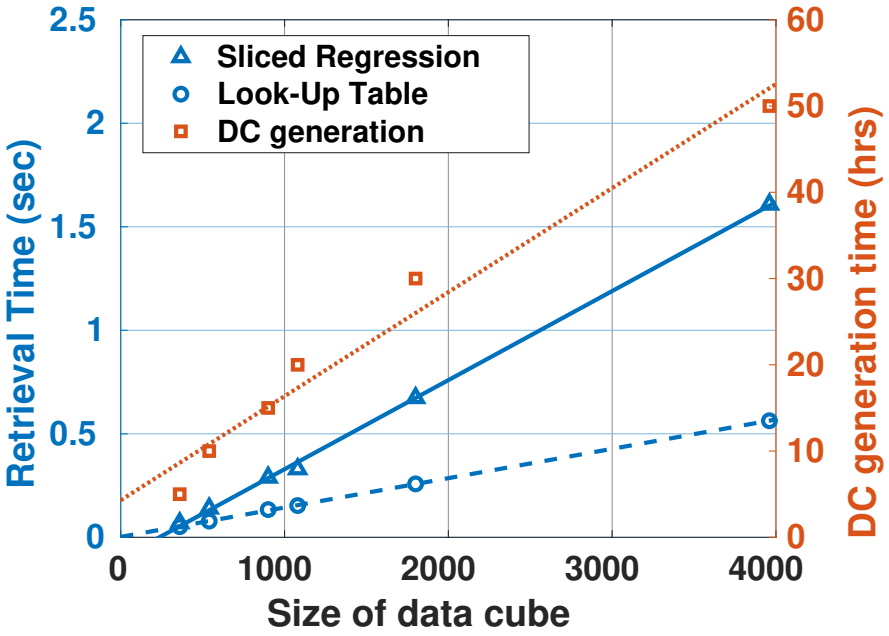

Figure 5.11: Comparison of retrieval time taken by SRI and LUT approach as well as data cube generation time for various sizes of data cube, with linear fits used to model the appropriate relationships.

CHAPTER 6

TIME SERIES APPROACH

6.1 Introduction

In this chapter, we discuss the various time series approach to retrieve soil moisture and how it helps in increasing the accuracy of snapshot retrieval. Various time series approaches have been introduced in the past that seek to retrieve soil moisture from radar backscatter data of multiple time snaps. Some of these popular techniques include (Kim and van Zyl, 2009; Ouellette *et al.*, 2017; Al-Khaldi *et al.*, 2019).

6.2 Partial Derivative based Approach

We discuss the time series estimation of soil moisture using the backscatter coefficients as presented in (van Zyl, 2011). Over time, the moisture content in the soil as well as the vegetation change with the amount of rainfall and other weather conditions. However, the soil roughness, as well as the vegetation geometrical structure, doesn't change much in comparison. This change in moisture influences the radar backscatter which can be written as

$$\Delta\sigma^{pq,f} = \frac{\partial F}{\partial mv}\Delta mv + \frac{\partial F}{\partial vm}\Delta vm \tag{6.1}$$

where Δmv and Δvm is the change in soil moisture and vegetation moisture respectively. F is the forward model function used to calculate the backscattering coefficient i.e. $\sigma^{pq,f} = F(h, l, mv, vm, pq, f)$. In case of NISAR operating bands which has two frequencies - L and S, and three polarizations HH, HV and VV, the absolute change in moisture content Δmv and Δvm can be calculated from the six radar measurements

by solving the matrix equation Eqn. 6.2.

$$\underbrace{\begin{pmatrix} \Delta\sigma^{HH,L} \\ \Delta\sigma^{VV,L} \\ \Delta\sigma^{HH,S} \\ \Delta\sigma^{VV,S} \\ \Delta\sigma^{HV,L} \\ \Delta\sigma^{HV,S} \end{pmatrix}}_{\mathbf{b}} = \underbrace{\begin{pmatrix} F_m^{HH,L} & F_v^{HH,L} \\ F_m^{VV,L} & F_v^{VV,L} \\ F_m^{HH,S} & F_v^{HH,S} \\ F_m^{VV,S} & F_v^{VV,S} \\ F_m^{HV,L} & F_v^{HV,L} \\ F_m^{HV,S} & F_v^{HV,S} \end{pmatrix}}_{\mathbf{A}} \underbrace{\begin{pmatrix} \Delta mv \\ \Delta vm \end{pmatrix}}_{\mathbf{x}} \tag{6.2}$$

where the partial derivatives $\partial F^{pq,f}/\partial mv$ and $\partial F^{pq,f}/\partial vm$ are denoted by $F_m^{pq,f}$ and $F_v^{pq,f}$ for frequency f and transmit-receive polarization pq.

The solution of Eqn. 6.2 is given by $\mathbf{x} = (A^T A)^{-1} A^T b$. We apply the SRI algorithm for the radar measurments at the first time snapshot and we call the retrieved sets of parameter $\mathbf{x}_{t_0}$. We now use these changes in soil moisture and vegetation moisture Δmv and Δvm for calculating the initial estimates $\mathbf{x}_0$ for the SRI algorithm as follows:

$$\begin{pmatrix} h \\ l \\ mv + \Delta mv \\ vm + \Delta vm \end{pmatrix} = \begin{pmatrix} h \\ l \\ mv \\ vm \end{pmatrix} + \begin{pmatrix} 0 \\ 0 \\ \Delta mv \\ \Delta vm \end{pmatrix} \tag{6.3}$$

OR

$$\mathbf{x}_0 = \mathbf{x}_{t_0} + \begin{pmatrix} 0 \\ 0 \\ \Delta mv \\ \Delta vm \end{pmatrix} \tag{6.4}$$

For the next time snap $t = t_0$, the soil and vegetation parameters can be retrieved by solving the following constrained optimization equation:

$$\begin{aligned} \underset{x}{\text{minimize}} \quad & \frac{1}{c_1}||\boldsymbol{\beta}\mathbf{x} - \mathbf{y}||_2^2 + \gamma \frac{1}{c_2} \|\mathbf{x} - \mathbf{x_0}\|_2^2 \\ \text{subject to} \quad & \mathbf{lb} \leq \mathbf{x} \leq \mathbf{ub} \quad \text{for each bin} \end{aligned} \tag{6.5}$$

where γ is the regularization parameter which is empirically determined, $c_1 = ||b||$, $c_2 = ||x||$ are the normalizing constant and lb and ub are the bounds of each bin in the

data cube. The regression coefficients $\boldsymbol{\beta}$ and the radar measurements $\mathbf{y}$ are defined by

$$\boldsymbol{\beta} = \begin{pmatrix} \beta_1^{HH,L} & \beta_2^{HH,L} & \beta_3^{HH,L} & \beta_4^{HH,L} \\ \beta_1^{VV,L} & \beta_2^{VV,L} & \beta_3^{VV,L} & \beta_4^{VV,L} \\ \beta_1^{HH,S} & \beta_2^{HH,S} & \beta_3^{HH,S} & \beta_4^{HH,S} \\ \beta_1^{VV,S} & \beta_2^{VV,S} & \beta_3^{VV,S} & \beta_4^{VV,S} \\ \beta_1^{HV,L} & \beta_2^{HV,L} & \beta_3^{HV,L} & \beta_4^{HV,L} \\ \beta_1^{HV,S} & \beta_2^{HV,S} & \beta_3^{HV,S} & \beta_4^{HV,S} \end{pmatrix}, \ \mathbf{y} = \begin{pmatrix} \sigma^{HH,L} & \beta_0^{HH,L} \\ \sigma^{VV,L} & \beta_0^{VV,L} \\ \sigma^{HH,S} & \beta_0^{HH,S} \\ \sigma^{VV,S} & \beta_0^{VV,S} \\ \sigma^{HV,L} & \beta_0^{HV,L} \\ \sigma^{HV,S} & \beta_0^{HV,S} \end{pmatrix}$$

Eqn. 6.5 can be solved by minimizing the following objective function with respect to variable $\mathbf{x}$ as follows:

$$\phi(\mathbf{x}) = \frac{1}{c_1}[\mathbf{x^T}(\mathbf{A^T A} + \gamma \mathbf{I})\mathbf{x} - \mathbf{2}(\mathbf{b^T A} + \gamma \mathbf{x_0^T})\mathbf{x} + \mathbf{b^T b}] + \frac{1}{c_1}\gamma \mathbf{x_0^T x_0} \tag{6.6}$$

6.3 Time Series with feedback

In this section, we discuss the time series approach that involves feedback from the previous time snapshots results. The retrieval algorithm for feedback time series consists of following steps:

1. Snapshot:
   Retrieve the initial values of parameters by solving the following equation

$$\begin{aligned} &\underset{x}{\text{minimize}} \quad ||\boldsymbol{\beta}\mathbf{x} - \mathbf{y}||_2^2 + \gamma \left\|\mathbf{x_m}\right\|_2^2 \\ &\text{subject to} \quad \mathbf{lb} \leq \mathbf{x} \leq \mathbf{ub} \quad \text{for each bin} \end{aligned} \tag{6.7}$$

   Estimates : $\mathbf{x_0} = [h_0, l_0, m_{v_0}, v_{m_0}]^T$.

2. Time-Series Update:
   (a) Update the moisture values keeping the soil geometrical properties constant.

$$m'_{v_0} = m_{v_0} + \Delta mv \tag{6.8}$$

$$v'_{m_0} = v_{m_0} + \Delta vm \tag{6.9}$$

   Estimates : $\mathbf{x'_0} = [h_0, l_0, m'_{v_0}, v'_{m_0}]^T$.
   (b) Use $\mathbf{x'_0}$ to find an estimate for the correct bin and refine the search.

- Update all variables ($\mathbf{x} = [h, l, mv, vm]^T$)

$$\begin{aligned} &\underset{x}{\text{minimize}} \quad ||\boldsymbol{\beta}\mathbf{x} - \mathbf{y}||_2^2 + \gamma \left\|\mathbf{x_m}\right\|_2^2 \\ &\text{subject to} \quad \mathbf{lb} \leq \mathbf{x} \leq \mathbf{ub} \quad \text{for the bins : [bin - } \Delta\text{, bin + } \Delta\text{]} \end{aligned} \tag{6.10}$$

where

$$\underbrace{\begin{pmatrix} \sigma^{HH,L} - \beta_0^{HH,L} \\ \sigma^{VV,L} - \beta_0^{VV,L} \\ \sigma^{HH,S} - \beta_0^{HH,S} \\ \sigma^{VV,S} - \beta_0^{VV,L} \\ \sigma^{HV,L} - \beta_0^{HV,L} \\ \sigma^{HV,S} - \beta_0^{HV,S} \end{pmatrix}}_{\mathbf{y}} = \underbrace{\begin{pmatrix} \beta_1^{HH,L} & \beta_2^{HH,L} & \beta_3^{HH,L} & \beta_4^{HH,L} \\ \beta_1^{VV,L} & \beta_2^{VV,L} & \beta_3^{VV,L} & \beta_4^{VV,L} \\ \beta_1^{HH,S} & \beta_2^{HH,S} & \beta_3^{HH,S} & \beta_4^{HH,S} \\ \beta_1^{VV,S} & \beta_2^{VV,S} & \beta_3^{VV,S} & \beta_4^{VV,S} \\ \beta_1^{HV,L} & \beta_2^{HV,L} & \beta_3^{HV,L} & \beta_4^{HV,L} \\ \beta_1^{HV,S} & \beta_2^{HV,S} & \beta_3^{HV,S} & \beta_4^{HV,S} \end{pmatrix}}_{\boldsymbol{\beta}} \underbrace{\begin{pmatrix} h \\ l \\ mv \\ vm \end{pmatrix}}_{\mathbf{x}} \tag{6.11}$$

Estimates : $\mathbf{x_{b1}} = [h_1, l_1, m_{v_1}, v_{m_1}]^T$

- Update only moisture values (mv and vm):
  Split $\mathbf{x}$ into moisture part $\mathbf{x_a}$ (unknown) and roughness part $\mathbf{x_b}$ (known) with $\mathbf{x_a} = [mv, vm]^T$ and $\mathbf{x_b} = [h, l]^T$.
  Run SRI algorithm for retrieving mv and vm based on the refined bin search.

$$\begin{aligned} &\underset{x}{\text{minimize}} \quad ||\boldsymbol{\beta_a}\mathbf{x_a} - \mathbf{y_0} - \mathbf{c}||_2^2 \\ &\text{subject to} \quad \mathbf{lb} \leq \mathbf{x_a} \leq \mathbf{ub} \quad \text{for the bins : [bin - } \Delta\text{, bin + } \Delta\text{]} \end{aligned} \tag{6.12}$$

where

$$\underbrace{\begin{pmatrix} \sigma^{HH,L} - \beta_0^{HH,L} \\ \sigma^{VV,L} - \beta_0^{VV,L} \\ \sigma^{HH,S} - \beta_0^{HH,S} \\ \sigma^{VV,S} - \beta_0^{VV,L} \\ \sigma^{HV,L} - \beta_0^{HV,L} \\ \sigma^{HV,S} - \beta_0^{HV,S} \end{pmatrix}}_{\mathbf{y}} + \underbrace{\begin{pmatrix} \beta_1^{HH,L}h + \beta_2^{HH,L}l \\ \beta_1^{VV,L}h + \beta_2^{VV,L}l \\ \beta_1^{HH,S}h + \beta_2^{HH,S}l \\ \beta_1^{VV,S}h + \beta_2^{VV,S}l \\ \beta_1^{HV,L}h + \beta_2^{HV,L}l \\ \beta_1^{HV,S}h + \beta_2^{HV,S}l \end{pmatrix}}_{\mathbf{c}} = \underbrace{\begin{pmatrix} \beta_3^{HH,L} & \beta_5^{HH,L} \\ \beta_3^{VV,L} & \beta_5^{VV,L} \\ \beta_3^{HH,S} & \beta_5^{HH,S} \\ \beta_3^{VV,S} & \beta_5^{VV,S} \\ \beta_3^{HV,L} & \beta_5^{HV,L} \\ \beta_3^{HV,S} & \beta_5^{HV,S} \end{pmatrix}}_{\boldsymbol{\beta_a}} \underbrace{\begin{pmatrix} mv \\ vm \end{pmatrix}}_{\mathbf{x_a}} \tag{6.13}$$

Estimates : $\mathbf{x_{b1}} = [h_0, l_0, m_{v_1}, v_{m_1}]^T$

3. Feedback to update h, l
   Split $\mathbf{x}$ into moisture part $\mathbf{x_a}$ (known) and roughness part $\mathbf{x_b}$ (unknown) with $\mathbf{x_a} = [mv, vm]^T$ and $\mathbf{x_b} = [h, l]^T$.
   Run SRI algorithm for retrieving mv and vm based on the refined bin search.

$$\begin{aligned} &\underset{x}{\text{minimize}} \quad ||\boldsymbol{\beta_b}\mathbf{x_b} - \mathbf{y_0} - \mathbf{c_0}||_2^2 + ||\boldsymbol{\beta_b}\mathbf{x_b} - \mathbf{y_1} - \mathbf{c_1}||_2^2 \\ &\text{subject to} \quad \mathbf{lb} \leq \mathbf{x_b} \leq \mathbf{ub} \quad \text{for each bin} \end{aligned} \tag{6.14}$$

where

$$\underbrace{\begin{pmatrix} \sigma_0^{HH,L} - \beta_0^{HH,L} \\ \sigma_0^{VV,L} - \beta_0^{VV,L} \\ \sigma_0^{HH,S} - \beta_0^{HH,S} \\ \sigma_0^{VV,S} - \beta_0^{VV,L} \\ \sigma_0^{HV,L} - \beta_0^{HV,L} \\ \sigma_0^{HV,S} - \beta_0^{HV,S} \end{pmatrix}}_{\mathbf{y_0}} + \underbrace{\begin{pmatrix} \beta_3^{HH,L} m_{v_0} + \beta_5^{HH,L} v_{m_0} \\ \beta_3^{VV,L} m_{v_0} + \beta_5^{VV,L} v_{m_0} \\ \beta_3^{HH,S} m_{v_0} + \beta_5^{HH,S} v_{m_0} \\ \beta_3^{VV,S} m_{v_0} + \beta_5^{VV,S} v_{m_0} \\ \beta_3^{HV,L} m_{v_0} + \beta_5^{HV,L} v_{m_0} \\ \beta_3^{HV,S} m_{v_0} + \beta_5^{HV,S} v_{m_0} \end{pmatrix}}_{\mathbf{c_0}} = \underbrace{\begin{pmatrix} \beta_1^{HH,L} & \beta_2^{HH,L} \\ \beta_1^{VV,L} & \beta_2^{VV,L} \\ \beta_1^{HH,S} & \beta_2^{HH,S} \\ \beta_1^{VV,S} & \beta_2^{VV,S} \\ \beta_1^{HV,L} & \beta_2^{HV,L} \\ \beta_1^{HV,S} & \beta_2^{HV,S} \end{pmatrix}}_{\boldsymbol{\beta_b}} \underbrace{\begin{pmatrix} h \\ l \end{pmatrix}}_{\mathbf{x_b}} \tag{6.15}$$

and

$$\underbrace{\begin{pmatrix} \sigma_1^{HH,L} - \beta_0^{HH,L} \\ \sigma_1^{VV,L} - \beta_0^{VV,L} \\ \sigma_1^{HH,S} - \beta_0^{HH,S} \\ \sigma_1^{VV,S} - \beta_0^{VV,L} \\ \sigma_1^{HV,L} - \beta_0^{HV,L} \\ \sigma_1^{HV,S} - \beta_0^{HV,S} \end{pmatrix}}_{\mathbf{y_1}} + \underbrace{\begin{pmatrix} \beta_3^{HH,L} m_{v_1} + \beta_5^{HH,L} v_{m_1} \\ \beta_3^{VV,L} m_{v_1} + \beta_5^{VV,L} v_{m_1} \\ \beta_3^{HH,S} m_{v_1} + \beta_5^{HH,S} v_{m_1} \\ \beta_3^{VV,S} m_{v_1} + \beta_5^{VV,S} v_{m_1} \\ \beta_3^{HV,L} m_{v_1} + \beta_5^{HV,L} v_{m_1} \\ \beta_3^{HV,S} m_{v_1} + \beta_5^{HV,S} v_{m_1} \end{pmatrix}}_{\mathbf{c_1}} = \underbrace{\begin{pmatrix} \beta_1^{HH,L} & \beta_2^{HH,L} \\ \beta_1^{VV,L} & \beta_2^{VV,L} \\ \beta_1^{HH,S} & \beta_2^{HH,S} \\ \beta_1^{VV,S} & \beta_2^{VV,S} \\ \beta_1^{HV,L} & \beta_2^{HV,L} \\ \beta_1^{HV,S} & \beta_2^{HV,S} \end{pmatrix}}_{\boldsymbol{\beta_b}} \underbrace{\begin{pmatrix} h \\ l \end{pmatrix}}_{\mathbf{x_b}} \tag{6.16}$$

Estimates : $\mathbf{x_f} = [h_f, l_f, m_{v_1}, v_{m_1}]^T$ Thus we get the final estimate of the parameter after applying the feedback time series mechanism

6.4 Multiple Cost Functions Approach

In this section, we use the time series approach proposed in (Kim and van Zyl, 2009) to retrieve soil moisture. The transition rate factor is assumed to be a constant i.e. $m = 0$ and hence it is not retrieved in the inversion process. The algorithm can be summarized in following steps:

1. We split the unknown vector $\mathbf{x}$ into the moisture part $\mathbf{x_a}$ (variable) and the roughness part $\mathbf{x_b}$ (fixed), where $\mathbf{x_a} = [mv, vm]^T$ and $\mathbf{x_b} = [h, l]^T$.

2. Considering all possible combinations of $\mathbf{x_b} = [h, l]^T$, we find the optimal value of (h, l) which minimizes the cost function $C(\mathbf{x_a}, \mathbf{x_b})$:

$$\tilde{C}(\mathbf{x_a}) = \underset{\mathbf{x_b}}{\text{minimize}}\, C(\mathbf{x_a}, \mathbf{x_b}) \tag{6.17}$$

where $C(x_a, x_b) = \sum_i^N ||\boldsymbol{\beta_a} \mathbf{x_{a_i}} - \mathbf{y_i} - \mathbf{c}||_2^2$ and N is the total number of time snaps. The vectors $\boldsymbol{\beta_a}, \mathbf{x_{a_i}}, \mathbf{y_i}, \mathbf{c}$ are given by

$$\mathbf{y}_i = \begin{pmatrix} \sigma_i^{HH,L} - \beta_0^{HH,L} \\ \sigma_i^{VV,L} - \beta_0^{VV,L} \\ \sigma_i^{HH,S} - \beta_0^{HH,S} \\ \sigma_i^{VV,S} - \beta_0^{VV,L} \\ \sigma_i^{HV,L} - \beta_0^{HV,L} \\ \sigma_i^{HV,S} - \beta_0^{HV,S} \end{pmatrix}, \mathbf{c} = \begin{pmatrix} \beta_1^{HH,L} & \beta_2^{HH,L} \\ \beta_1^{VV,L} & \beta_2^{VV,L} \\ \beta_1^{HH,S} & \beta_2^{HH,S} \\ \beta_1^{VV,S} & \beta_2^{VV,S} \\ \beta_1^{HV,L} & \beta_2^{HV,L} \\ \beta_1^{HV,S} & \beta_2^{HV,S} \end{pmatrix} \begin{pmatrix} h \\ l \end{pmatrix}$$

$$\boldsymbol{\beta_a} = \begin{pmatrix} \beta_3^{HH,L} & \beta_5^{HH,L} \\ \beta_3^{VV,L} & \beta_5^{VV,L} \\ \beta_3^{HH,S} & \beta_5^{HH,S} \\ \beta_3^{VV,S} & \beta_5^{VV,S} \\ \beta_3^{HV,L} & \beta_5^{HV,L} \\ \beta_3^{HV,S} & \beta_5^{HV,S} \end{pmatrix}, \mathbf{x_{a_i}} = \begin{pmatrix} m_{v_i} \\ v_{m_i} \end{pmatrix}$$

3. We now proceed to find the optimal value of moisture mv, vm by minimizing the new cost function $\tilde{C}(\mathbf{x_b})$. We solve the following the optimization equation:

$$\begin{aligned} &\underset{\mathbf{x_a}}{\text{minimize}} \quad ||\boldsymbol{\beta_a}\mathbf{x_a} - \mathbf{y_0} - \mathbf{c}||_2^2 \\ &\text{subject to} \quad \mathbf{lb} \leq \mathbf{x_a} \leq \mathbf{ub} \quad \text{for all bins} \end{aligned} \tag{6.18}$$

   Since the data cube has only two axis in this case, thus the lower and upper bounds of a bin are the corresponding soil and vegetation moisture values i.e.

$$\mathbf{lb} = \begin{pmatrix} m_{v_1} \\ v_{m_1} \end{pmatrix}, \quad \mathbf{ub} = \begin{pmatrix} m_{v_2} \\ v_{m_2} \end{pmatrix}$$

4. Retrieved estimates of soil moisture mv and vegetation moisture vm are the corresponding x_a.

CHAPTER 7

CONCLUSION

We have presented a novel physics-based soil moisture retrieval technique called the Sliced Regression Inversion Algorithm which is based on an electromagnetic scattering model. The algorithm uses multi-polarized multi-frequency SAR backscatter data to retrieve soil moisture by using a data cube of backscatter coefficients generated by a physics-based forward model. Our proposed SRI algorithm is based on the fact that any linear model can be inverted provided sufficient measurements are available. The algorithm is modular in nature, thus it allows the fusion of backscatter data from multiple frequency bands and polarizations. The algorithm will be crucial for the upcoming NASA-ISRO joint mission termed NISAR (Rosen *et al.*, 2017).

We used the Improved Integral Equation Model (I^2EM) for simulating the multi-pol and multi-band backscatter from bare soil. We also extended this model to incorporate depth-dependent soil moisture by assuming a vertical dielectric profile. The radar backscatter from heterogeneous soil surface was calculated by modifying the reflection coefficients in the I^2EM model. The effects of vegetation was included by modelling it as a collection of randomly oriented dielectric cylinders with its orientation dictated by a probability density function. Finally, the radar backscatter was calculated by taking the ensemble average of scattering coefficients of all the scatterers. Since the data cube for the SRI algorithm is generated using physics-based scattering models, our algorithm has a broader range of applicability than the empirical models.

The SRI algorithm was applied to both real as well as synthetically generated datasets and the performance of the algorithm was evaluated in terms of root mean squared error (RMSE). First, we showed that the SRI for bare soil works better than the existing SMART Inversion Model in terms of retrieval accuracy. We applied the SRI algorithm for retrieval using the NISAR operating bands information(L and S) and observed that using the co-polarized dual-band combination of backscattering coefficients gives the best accuracy. We also showed that SRI gives better accuracy than the lookup table approach when applied to the backscatter information collected at L-band from the ALOS

PALSAR sensor (HH and HV), and C-band from the SENTINEL-1A sensor (VV and VH). For the experimental dataset, we obtained a retrieval accuracy of 0.06 cm^3/cm^3 for bare soils and an RMSE of 0.14-0.18 cm^3/cm^3 for vegetated lands i.e. maize, chilli and jowar. The time series approach discussed didn't yield better results than the snap-shot SRI algorithm. Thus further study is needed on how to improve the existing time series approaches to retrieve soil moisture. It is to be noted that while the algorithm delivers soil moisture retrievals over the field-scale, the radar observations are on a larger length scale. Recent work (Ma *et al.*, 2019) has shown that the discrepancy between model retrievals and radar data can often be caused due to these scaling issues.

APPENDIX A

VEGETATION SCATTERING MODEL

In this chapter, we will discuss the details of vegetation scattering model and derive the scattering coefficients of a single cylinder with arbitrary orientation. We use the formulation given in this book (van Zyl, 2011) to derive the coefficients.

A.1 Coordinate System and Angles

First, we refer to all angles in two coordinate systems: global coordinates and the coordinates relative to the cylinder.

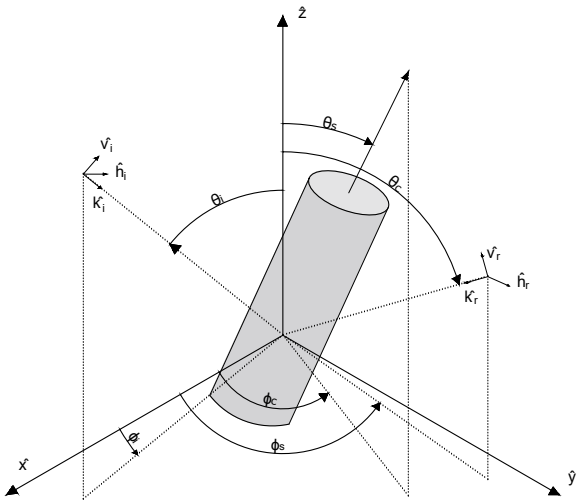

Figure A.1: Global Backscattering Alignment Coordinate System

The angles in the Figure A.1 are defined as follows:

- θ_i : Polar Incident Angle of the incident wave
- ϕ_i : Azimuthal Incident Angle of the incident wave
- θ_s : Polar Scattered Angle of the scattered wave
- ϕ_s : Azimuthal Scattered Angle of the scattered wave
- θ_c : Polar Angle of the Normal to the Cylinder

- ϕ_c: Azimuthal Angle of the Normal to the Cylinder

Now consider the zenith direction to be shifted from the z-axis to the vector $\hat{c}$, i.e the normal to the cylinder. This will define the angles relative to the cylinder. The polar angles will be redefined, but the azimuthal angles remain the same.

- θ_{ic} : 'Relative' Polar Incident Angle of the incident wave

$$\cos\theta_{ic} = \cos\ \theta_c \cos\ \theta_i + \sin\theta_c\theta_i \cos\left(\phi_c - \phi_i\right) \tag{A.1}$$

- θ_{sc} : 'Relative' Scattered Angle of the scattered wave

$$\cos\theta_{sc} = \cos\ \theta_c \cos\ \theta_s + \sin\theta_c\theta_s \cos\left(\phi_c - \phi_s\right) \tag{A.2}$$

A.2 Scattering Matrix of an Arbitrary Oriented Dielectric Cylinder

The bistatic scattering matrix contains the scattering coefficients that gives the relation between the incident field and the scattered field. The corresponding matrix equation is defined as follows:

$$\mathbf{E}^{sc} = [\mathbf{S}]\mathbf{E}^{inc}\frac{e^{ikr}}{r}$$

where

$$\mathbf{S} = \begin{pmatrix} S_{HH} & S_{HV} \\ S_{VH} & S_{VV} \end{pmatrix},\ \mathbf{E}^{sc} = \begin{pmatrix} E^{sc}_{HH} \\ E^{sc}_{VV} \end{pmatrix},\ \mathbf{E}^{inc} = \begin{pmatrix} E^{inc}_{HH} \\ E^{inc}_{VV} \end{pmatrix}$$

First, we shall establish the terms of the scattering matrix for a vertically oriented cylinder where the cylinder orientation aligns with the z-axis (Figure 3.1). In this case, the angles relative to the global coordinates and the angles relative to the cylinder coincide. The elements of the scattering matrices, as a function of incidence and scattered

angle, are given by (van Zyl, 2011):

$$S_{HH}(\theta_i, \phi_i, \theta_s, \phi_s) = -\frac{il \sin\ \theta_s}{\pi \sin\ \theta_i} \frac{\sin\ V}{V} \sum_{m=-\infty}^{+\infty} \left\{(-1)^m C_m^{TM} e^{im(\phi_s - \phi_i)}\right\} \tag{A.3}$$

$$S_{HV}(\theta_i, \phi_i, \theta_s, \phi_s) = -\frac{il \sin\ \theta_s}{\pi \sin\ \theta_i} \frac{\sin\ V}{V} \sum_{m=-\infty}^{+\infty} \left\{(-1)^m \bar{C}_m e^{im(\phi_s - \phi_i)}\right\} \tag{A.4}$$

$$S_{VH}(\theta_i, \phi_i, \theta_s, \phi_s) = +\frac{il \sin\ \theta_s}{\pi \sin\ \theta_i} \frac{\sin\ V}{V} \sum_{m=-\infty}^{+\infty} \left\{(-1)^m \bar{C}_m e^{im(\phi_s - \phi_i)}\right\} \tag{A.5}$$

$$S_{VV}(\theta_i, \phi_i, \theta_s, \phi_s) = -\frac{il \sin\ \theta_s}{\pi \sin\ \theta_i} \frac{\sin\ V}{V} \sum_{m=-\infty}^{+\infty} \left\{(-1)^m C_m^{TE} e^{im(\phi_s - \phi_i)}\right\} \tag{A.6}$$

where

$$x_0 = k_0 a \sin\ \theta_i \tag{A.7}$$

$$x_1 = k_0 a \sqrt{\epsilon - \cos^2\ \theta_i} \tag{A.8}$$

$$q_m = m k_0 a \cos\ \theta_i \left(\frac{1}{x_1^2} - \frac{1}{x_0^2}\right) \tag{A.9}$$

$$vm = k_0 a \left(\frac{\epsilon}{x_1} J_m(x_0) J_m'(x_1) - \frac{1}{x_0} J_m'(x_0) J_m(x_1)\right) \tag{A.10}$$

$$P_m = k_0 a \left(\frac{1}{x_1} H_m^{(1)}(x_0) J_m'(x_1) - \frac{1}{x_0} H_m^{(1)'}(x_0) J_m(x_1)\right) \tag{A.11}$$

$$N_m = k_0 a \left(\frac{\epsilon}{x_1} H_m^{(1)}(x_0) J_m'(x_1) - \frac{1}{x_0} H_m^{(1)'}(x_0) J_m(x_1)\right) \tag{A.12}$$

$$M_m = k_0 a \left(\frac{1}{x_1} J_m(x_0) J'_m(x_1) - \frac{1}{x_0} J'_m(x_0) J_m(x_1) \right) \tag{A.13}$$

$$V = \frac{1}{2} k_0 l (\cos\ \theta_i + \cos\ \theta_s) \tag{A.14}$$

$$C_m^{TM} = -\frac{vmP_m - q_m^2 J_m(x_0) H_m^{(1)}(x_0) J_m^2(x_1)}{P_m N_m - \left[q_m H_m^{(1)}(x_0) J_m(x_1) \right]^2} \tag{A.15}$$

$$C_m^{TE} = -\frac{M_m N_m - q_m^2 J_m(x_0) H_m^{(1)}(x_0) J_m^2(x_1)}{P_m N_m - \left[q_m H_m^{(1)}(x_0) J_m(x_1) \right]^2} \tag{A.16}$$

$$\bar{C_m} = i \frac{2}{\pi x_0 \sin\ \theta_i} \frac{q_m J_m^2(x_1)}{P_m N_m - \left[q_m H_m^{(1)}(x_0) J_m(x_1) \right]^2} \tag{A.17}$$

To extend this to an arbitrary orientation of the cylinder, we first move the frame of coordinates relative to the cylinder. In this frame, our incident and scattered angles are $\theta_{\mathbf{ic}}$ and $\theta_{\mathbf{sc}}$ respectively. In this frame, the scattering matrix is still being defined for a vertical cylinder. Therefore, we can use Eqn. A.3, A.6, A.4 to arrive at the relative scattering matrix, in the local coordinates defined by $S(\theta_{ic}, \phi_i, \theta_{sc}, \phi_s)$.

Therefore:

$$\begin{pmatrix} E_{h'} \\ E_{v'} \end{pmatrix}^{sc} = S(\theta_{ic}, \phi_i, \theta_{sc}, \phi_s) \begin{pmatrix} E_{h'} \\ E_{v'} \end{pmatrix}^{inc}$$

where the primed notation represents the local coordinates, and the unprimed notation represents the global coordinates.

$$\begin{pmatrix} E_h \\ E_v \end{pmatrix}^{sc} = \begin{pmatrix} h_s \cdot h'_s & h_s \cdot v'_s \\ v_s \cdot h'_s & v_s \cdot v'_s \end{pmatrix} \begin{pmatrix} E_{h'} \\ E_{v'} \end{pmatrix}^{sc}$$

It follows immediately that the global bistatic scattering matrix of an arbitrary ori-

entation is given by

$$\mathbf{S}(\theta_i, \phi_i, \theta_s, \phi_s, \theta_c, \phi_c) = \begin{pmatrix} \mathbf{h}_s \cdot \mathbf{h}'_s & \mathbf{h}_s \cdot \mathbf{v}'_s \\ \mathbf{v}_s \cdot \mathbf{h}'_s & \mathbf{v}_s \cdot \mathbf{v}'_s \end{pmatrix} \mathbf{S}(\theta_{ic}, \phi_i, \theta_{sc}, \phi_s) \begin{pmatrix} \mathbf{h}_i \cdot \mathbf{h}'_i & \mathbf{h}_i \cdot \mathbf{v}'_i \\ \mathbf{v}_i \cdot \mathbf{h}'_i & \mathbf{v}_i \cdot \mathbf{v}'_i \end{pmatrix} \tag{A.18}$$

where

$$\mathbf{h}_i \cdot \mathbf{h}'_i = \mathbf{v}_i \cdot \mathbf{v}'_i = \frac{1}{\sin\ \theta_{ic}} \{\cos\ \theta_c \sin\theta_i - \sin\theta_c \cos\theta_i \cos(\phi_c - \phi_i)\} \tag{A.19}$$

$$\mathbf{h}_i \cdot \mathbf{v}'_i = -\mathbf{v}_i \cdot \mathbf{h}'_i = -\frac{\sin\ \theta_c \sin(\phi_c - \phi_i)}{\sin\theta_{ic}} \tag{A.20}$$

$$\mathbf{h}_s \cdot \mathbf{h}'_s = \mathbf{v}_s \cdot \mathbf{v}'_s = \frac{1}{\sin\ \theta_{sc}} \{\cos\ \theta_c \sin\theta_s - \sin\theta_c \cos\theta_s \cos(\phi_c - \phi_s)\} \tag{A.21}$$

$$\mathbf{h}_s \cdot \mathbf{v}'_s = -\mathbf{v}_s \cdot \mathbf{h}'_s = -\frac{\sin\ \theta_c \sin(\phi_c - \phi_s)}{\sin\theta_{sc}} \tag{A.22}$$

A.3 Probability Density Function

For this model, we have assumed a cosine squared probability density function $p(\theta_c, \phi_c)$ which is given by

$$\int_0^{2\pi} \int_0^{\pi} p(\theta_c, \phi_c)\ \sin\ \theta_c\ d\theta_c\ d\phi_c = 1 \tag{A.23}$$

A cosine squared distribution about the vertical implies that the cylinders are more likely to be oriented close to the vertical (Arii, 2009). This is true for most crops, where the stalks are oriented at small angles about the vertical.

$$p(\theta_c, \phi_c) = \frac{1}{A} \cos^2\theta_c \cos^2\phi_c \tag{A.24}$$

where A is the normalizing constant.

This probability density function will used to calculate the ensemble average $\langle x \rangle$ of

any variable $x(\theta, \phi)$ given by

$$\langle x \rangle = \int_0^{2\pi} \int_0^{\pi} x(\theta, \phi)\, p(\theta, \phi) \sin\theta \, d\theta \, d\phi \tag{A.25}$$

A.4 Extinction Coefficient

The extinction coefficient characterizes the attenuation suffered by the incident wave when it passes through the vegetation layer. It is directly related to dielectric constant for the vegetation layer of randomly oriented cylinders. This attenuation through the layer is calculated using the optical theorem (Hulst and van de Hulst, 1981) which states that extinction cross-section of a single particle is related to scattering coefficient as follows:

$$\sigma_p^e = \frac{2\pi}{k_0} \mathsf{Im}\left[S_{pp}(\theta_{ic}, \phi_i, \pi - \theta_{ic}, \phi_i + \pi, \theta_c, \phi_c)\right] \tag{A.26}$$

where σ_p^e is the extinction cross-section of a single particle and p is the polarization which can be either horizontal or vertical (van Zyl, 2011). The total extinction coefficient κ_e^p is calculated by taking the ensemble average of the extinction cross-section is performed for all the particles.

$$\kappa_p^e = N\langle \sigma_p^e \rangle = \int_0^{2\pi} \int_0^{\pi} \sigma_p^e\, p(\theta, \phi) \sin\theta \, d\theta \, d\phi \tag{A.27}$$

where N is the density of scatterers in cylinders/m^3.

Now we can define the total vertical optical depth for the two polarizations as (van Zyl, 2011)

$$\tau_{hm} = \kappa_h^e b \quad \tau_{vm} = \kappa_v^e b$$

In general, however, the average optical path depth at a height z from the ground is given by

$$\tau_p = \frac{\kappa_p^e (b - z)}{cos\theta_i}$$

Using this notion of an effective dielectric slab described by the extinction coefficient, we can say that the strength of the incident wave after propagating through a layer of thickness d at an angle θ_i with respect to the vertical direction, is given by

$$\begin{pmatrix} E_h \\ E_v \end{pmatrix}^{tr} = \begin{pmatrix} e^{-\kappa_h^e d/\cos\theta_i} & 0 \\ 0 & e^{-\kappa_v^e d/\cos\theta_i} \end{pmatrix} \begin{pmatrix} E_h \\ E_v \end{pmatrix}^{inc} \tag{A.28}$$

A.5 Vegetation Dielectric Constant

The dielectric constant of the cylinder is directly related to the moisture content in the vegetation. It is computed as the sum of nondispersive, bound and free water components weighted appropriately by their volume fractions (van Zyl, 2011; Ulaby and El-Rayes, 1987).

$$\epsilon_v = \epsilon_r + v_{fw}\epsilon_f + v_b\epsilon_b \tag{A.29}$$

where

- ϵ_v is the vegetation dielectric constant
- ϵ_r is the non-dispersive residual part of the dielectric constant
- ϵ_f is the dielectric constant of free water
- v_{fw} is the volume fraction of free water
- ϵ_b is the dielectric constant of bound water
- v_b is the volume fraction of vegetation bound water
- vm is the vegetation moisture

The definitions of these parameters is given below.

$$\epsilon_r = 1.7 + 3.2vm + 6.5vm^2 \tag{A.30}$$

$$v_{fw} = vm[0.82vm + 0.166] \tag{A.31}$$

$$\epsilon_f = 4.9 + \frac{75}{1 + jf/18} - j\frac{18\sigma_{sal}}{f} \tag{A.32}$$

$$\sigma_{sal} = 0.16S - 0.0013S^2 \tag{A.33}$$

where

- S is the **salinity of the water** measured in parts per thousand on a weight basis
- f is the **frequency in Gigahertz**

The volume fraction of bound water is given by

$$v_b = \frac{31.4mv^2}{1 + 59.5mv^2} \tag{A.34}$$

The dielectric constant of bound water is

$$\epsilon_b = 2.9 + \frac{55}{1 + \sqrt{jf/0.18}} \tag{A.35}$$

APPENDIX B

Details of SAR data and ground truth collection

B.1 Study Area

The Agriculture fields spread over Guntur, Andhra Pradesh, India, were selected as study sites during the ISRO Airborne L&S-band SAR campaign for in-situ measurements from 22 Feb to 2 March 2018 by Space Applications Centre (ISRO) and other teams. Tropical climate conditions with extremely hot summer and cold winter prevail in the Guntur District. The climate of the district is moderate and characterized by tropical rainy climate with an aggressive summer. During the study period, the annual average minimum and maximum temperatures of the district are 20.6^o C and 33.5^o C, respectively. The average annual rainfall of the district during this period is 5 mm. The predominant crops cultivated in the district are paddy, jowar, and bajra among cereals; tobacco, cotton, and chilies among non-food and commercial crops; and black gram and red gram among pulses. Figure B.1 shows the field campaign over Vijayawada and Guntur study area in Feb-Mar, 2018 over (a) Maize Crop, (b) Chilli Crop, and (c) Bare Soil.

Figure B.1: Ground truth data collection field sites: (a) Maize Crop, (b) Chilli Crop, (c) Bare Soil

B.2 Sentinel-1 SAR Data

The C-band data used here is Sentinel-1 Level-1 Ground Range Detected High resolution (GRDH) with dual (VV+VH) polarization. The data was acquired on 1 March

2018, with the so-called interferometric wide swath mode at a spatial resolution of 5 $\times$ 20 m, and a swath width of 250 km. The Sentinel-1 image of the study area was processed using Sentinel Application Platform (SNAP) V7.0 in order to generate Radiometric Terrain Corrected (RTC) calibrated backscatter (σ^0) for both VV and VH polarization. The pre-processing steps of Sentinel-1 data are as follows: (1) application of orbit file to correct orbit, (2) multi-Look processing, (3) border noise removal, (4) radiometric calibration, (5) filtering and denoising processing (refined-Lee filtering, 3 pixels by 3 pixel window) to eliminate speckle noise, (6) linear to dB scale conversion, and (7) geocoding using digital elevation maps for geometric fine correction. Finally, the mean backscatter coefficient (σ^0) for both VV and VH polarization channels was computed over field sampling points on the same date of pass for further retrieval and analysis.

B.3 ALOS-2 PALSAR Data

The L-band data used here was acquired by the Phased Array Synthetic Aperture Radar (PALSAR) payload of ALOS-2 (Advanced Land Observing Satellite). The dual-polarized data (HH+HV) with pixel size of 25x25 m and spatial resolution of 100m was acquired on 28 Feb 2018, in Level 1.5 CEOS format. This data was processed in ScanSAR mode using the Sentinel Application Platform (SNAP) V7.0 in order to generate Radiometric Terrain Corrected (RTC) calibrated backscatter (σ^0) for both HH and HV polarizations and projected in WGS 1984 Universal Transverse Mercator (UTM) coordinates with 30-meter pixel size. A 30-meter Digital Elevation Model (DEM) from Shuttle Radar Topography Mission (SRTM) data was used for terrain correction over selected study sites. The mean backscatter coefficient for both HH and HV polarization channels was computed over field sampling points on the same date of pass for further retrieval and analysis.

B.4 In-situ Data

During the field campaign, more than 221 sample field points were covered with measurements of surface soil moisture, soil temperature, electrical conductivity (EC), soil

roughness and crop parameters (such as the stage of growth, density, height, leaf per plant and vigor, etc.). Soil measurements were performed using the Hydra Probe (POGO) handheld soil probe which measures volumetric soil moisture(%), soil temperature, and electrical conductivity. The major crops were Maize, Jowar, Chilli, Green gram and Tobacco during field campaign, while the minor crops were Shorgum, Chickpea, fodder, and vegetables. Most of the fields were in a very dry state with soil moisture varying from 3% to 20%. Some of the fields were irrigated and waterlogged.

REFERENCES

1. **Al-Khaldi, M. M.**, **J. T. Johnson**, **A. J. O'Brien**, **A. Balenzano**, and **F. Mattia** (2019). Time-series retrieval of soil moisture using cygnss. *IEEE Transactions on Geoscience and Remote Sensing*.

2. **Alemohammad, S. H.**, **T. Jagdhuber**, **M. Moghaddam**, and **D. Entekhabi** (2019). Soil and vegetation scattering contributions in l-band and p-band polarimetric sar observations. *IEEE Transactions on Geoscience and Remote Sensing*, **57**(11), 8417–8429.

3. **Allen, B. D.**, **S. A. Braun**, **J. H. Crawford**, **E. J. Jensen**, **C. E. Miller**, **M. Moghaddam**, and **H. Maring**, Proposed investigations from nasa's earth venture-1 (ev-1) airborne science selections. *In 2010 IEEE International Geoscience and Remote Sensing Symposium*. IEEE, 2010.

4. **Arii, M.** (2009). *Retrieval of soil moisture under vegetation using polarimetric radar*. Ph.D. thesis, California Institute of Technology.

5. **Attema, E.** and **F. T. Ulaby** (1978). Vegetation modeled as a water cloud. *Radio science*, **13**(2), 357–364.

6. **Beckmann, P.** and **A. Spizzichino** (1987). The scattering of electromagnetic waves from rough surfaces. *Norwood, MA, Artech House, Inc., 1987, 511 p.*.

7. **Bindlish, R.** and **A. P. Barros** (2001). Parameterization of vegetation backscatter in radar-based, soil moisture estimation. *Remote sensing of environment*, **76**(1), 130–137.

8. **Boyd, S.**, **N. Parikh**, **E. Chu**, **B. Peleato**, **J. Eckstein**, *et al.* (2011). Distributed optimization and statistical learning via the alternating direction method of multipliers. *Foundations and Trends® in Machine learning*, **3**(1), 1–122.

9. **Brekhovskikh, L.**, *Waves in layered media*, volume 16. Elsevier, 2012.

10. **Broschat, S. L.** (1993). The small slope approximation reflection coefficient for scattering from a" pierson-moskowitz" sea surface. *IEEE Transactions on Geoscience and Remote Sensing*, **31**(5), 1112–1114.

11. **Burgin, M. S.**, **U. K. Khankhoje**, **X. Duan**, and **M. Moghaddam** (2016). Generalized terrain topography in radar scattering models. *IEEE Transactions on Geoscience and Remote Sensing*, **54**(7), 3944–3952.

12. **Chapin, E.**, **A. Chau**, **J. Chen**, **B. Heavey**, **S. Hensley**, **Y. Lou**, **R. Machuzak**, and **M. Moghaddam**, Airmoss: An airborne p-band sar to measure root-zone soil moisture. *In 2012 IEEE Radar Conference*. IEEE, 2012.

13. **Chen, K.-S.**, **T.-D. Wu**, **L. Tsang**, **Q. Li**, **J. Shi**, and **A. K. Fung** (2003). Emission of rough surfaces calculated by the integral equation method with comparison to three-dimensional moment method simulations. *IEEE Transactions on Geoscience and Remote Sensing*, **41**(1), 90–101.

14. **Chen, K.-S.**, **T.-D. Wu**, **M.-K. Tsay**, and **A. K. Fung** (2000). Note on the multiple scattering in an iem model. *IEEE Transactions on Geoscience and Remote Sensing*, **38**(1), 249–256.

15. **Dave, R.**, **G. Kumar**, **D. K. Pandey**, **A. Khan**, and **B. Bhattacharya** (2019). Evaluation of modified dubois model for estimating surface soil moisture using dual polarization risat-1 c-band sar data. *Geocarto International*, **0**(0), 1–11. URL `https://doi.org/10.1080/10106049.2019.1655801`.

16. **De Roo, R. D.**, **Y. Du**, **F. T. Ulaby**, and **M. C. Dobson** (2001). A semi-empirical backscattering model at l-band and c-band for a soybean canopy with soil moisture inversion. *IEEE Transactions on Geoscience and Remote Sensing*, **39**(4), 864–872.

17. **Dobson, M. C.** and **F. T. Ulaby** (1986*a*). Active microwave soil moisture research. *IEEE Transactions on Geoscience and Remote Sensing*, **GE-24**(1), 23–36.

18. **Dobson, M. C.** and **F. T. Ulaby** (1986*b*). Preliminaly evaluation of the sir-b response to soil moisture, surface roughness, and crop canopy cover. *IEEE Transactions on Geoscience and Remote Sensing*, (4), 517–526.

19. **Dobson, M. C.**, **F. T. Ulaby**, **M. T. Hallikainen**, and **M. A. El-Rayes** (1985). Microwave dielectric behavior of wet soil-part ii: Dielectric mixing models. *IEEE Transactions on Geoscience and Remote Sensing*, **GE-23**(1), 35–46.

20. **Dubois, P. C.**, **J. Van Zyl**, and **T. Engman** (1995). Measuring soil moisture with imaging radars. *IEEE Transactions on Geoscience and Remote Sensing*, **33**(4), 915–926.

21. **Entekhabi, D.**, **E. G. Njoku**, **P. Houser**, **M. Spencer**, **T. Doiron**, **Y. Kim**, **J. Smith**, **R. Girard**, **S. Belair**, **W. Crow**, *et al.* (2004). The hydrosphere state (hydros) satellite mission: An earth system pathfinder for global mapping of soil moisture and land freeze/thaw. *IEEE Transactions on Geoscience and Remote Sensing*, **42**(10), 2184–2195.

22. **Entekhabi, D.**, **E. G. Njoku**, **P. E. O'Neill**, **K. H. Kellogg**, **W. T. Crow**, **W. N. Edelstein**, **J. K. Entin**, **S. D. Goodman**, **T. J. Jackson**, **J. Johnson**, *et al.* (2010). The soil moisture active passive (smap) mission. *Proceedings of the IEEE*, **98**(5), 704–716.

23. **Freeman, A.** and **S. L. Durden** (1998). A three-component scattering model for polarimetric sar data. *IEEE Transactions on Geoscience and Remote Sensing*, **36**(3), 963–973.

24. **Fung, A.**, **M. Dawson**, **K. Chen**, **A. Hsu**, **E. Engman**, **P. O'Neill**, and **J. Wang**, A modified iem model for: scattering from soil surfaces with application to soil moisture sensing. *In IGARSS'96. 1996 International Geoscience and Remote Sensing Symposium*, volume 2. IEEE, 1996.

25. **Fung, A.**, **W. Liu**, **K. Chen**, and **M. Tsay** (2002). An improved iem model for bistatic scattering from rough surfaces. *Journal of Electromagnetic Waves and Applications*, **16**(5), 689–702.

26. **Fung, A. K.** (1994). Microwave scattering and emission models and their applications.

27. **Fung, A. K.** and **K.-S. Chen** (2004). An update on the iem surface backscattering model. *IEEE Geoscience and Remote Sensing Letters*, **1**(2), 75–77.

28. **Fung, A. K.**, **K.-S. Chen**, and **K. Chen**, *Microwave scattering and emission models for users*. Artech house, 2010.

29. **Fung, A. K.**, **Z. Li**, and **K.-S. Chen** (1992). Backscattering from a randomly rough dielectric surface. *IEEE Transactions on Geoscience and remote sensing*, **30**(2), 356–369.

30. **Hajnsek, I.**, **E. Pottier**, and **S. R. Cloude** (2003). Inversion of surface parameters from polarimetric sar. *IEEE Transactions on Geoscience and Remote Sensing*, **41**(4), 727–744.

31. **Hallikainen, M. T.**, **F. T. Ulaby**, **M. C. Dobson**, **M. A. El-Rayes**, and **L.-K. Wu** (1985). Microwave dielectric behavior of wet soil-part 1: Empirical models and experimental observations. *IEEE Transactions on Geoscience and Remote Sensing*, (1), 25–34.

32. **Hulst, H. C.** and **H. C. van de Hulst**, *Light scattering by small particles*. Courier Corporation, 1981.

33. **Irisov, V.** (1997). Small-slope expansion for thermal and reflected radiation from a rough surface. *Waves in random media*, **7**(1), 1–10.

34. **Ishimaru, A.**, *Wave propagation and scattering in random media*, volume 2. Academic press New York, 1978.

35. **Jackson, T.** and **F. Schiebe** (1993). Washita'92 data report. *NAWQL report*, **101**.

36. **Johnson, J. T.** (2002). Comparison of the physical optics and small slope theories for polarimetric thermal emission from the sea surface. *IEEE transactions on geoscience and remote sensing*, **40**(2), 500–504.

37. **Kerr, Y. H.**, **P. Waldteufel**, **P. Richaume**, **J. P. Wigneron**, **P. Ferrazzoli**, **A. Mahmoodi**, **A. Al Bitar**, **F. Cabot**, **C. Gruhier**, **S. E. Juglea**, *et al.* (2012). The smos soil moisture retrieval algorithm. *IEEE Transactions on Geoscience and Remote Sensing*, **50**(5), 1384–1403.

38. **Kerr, Y. H.**, **P. Waldteufel**, **J.-P. Wigneron**, **J. Martinuzzi**, **J. Font**, and **M. Berger** (2001). Soil moisture retrieval from space: The soil moisture and ocean salinity (smos) mission. *IEEE transactions on Geoscience and remote sensing*, **39**(8), 1729–1735.

39. **Khankhoje, U. K.**, **J. J. van Zyl**, and **T. A. Cwik** (2012). Computation of radar scattering from heterogeneous rough soil using the finite-element method. *IEEE Transactions on Geoscience and Remote Sensing*, **51**(6), 3461–3469.

40. **Kim, S.-B.**, **M. Moghaddam**, **L. Tsang**, **M. Burgin**, **X. Xu**, and **E. G. Njoku** (2013). Models of l-band radar backscattering coefficients over global terrain for soil moisture retrieval. *IEEE Transactions on Geoscience and Remote Sensing*, **52**(2), 1381–1396.

41. **Kim, S.-B.**, **L. Tsang**, **J. T. Johnson**, **S. Huang**, **J. J. van Zyl**, and **E. G. Njoku** (2011). Soil moisture retrieval using time-series radar observations over bare surfaces. *IEEE Transactions on Geoscience and Remote Sensing*, **50**(5), 1853–1863.

42. **Kim, S.-B.**, **J. J. Van Zyl**, **J. T. Johnson**, **M. Moghaddam**, **L. Tsang**, **A. Colliander**, **R. S. Dunbar**, **T. J. Jackson**, **S. Jaruwatanadilok**, **R. West**, *et al.* (2017). Surface soil moisture retrieval using the l-band synthetic aperture radar onboard the soil moisture active–passive satellite and evaluation at core validation sites. *IEEE Transactions on Geoscience and Remote Sensing*, **55**(4), 1897–1914.

43. **Kim, Y.** and **J. J. van Zyl** (2009). A time-series approach to estimate soil moisture using polarimetric radar data. *IEEE Transactions on Geoscience and Remote Sensing*, **47**(8), 2519–2527.

44. **Kong, J. A.**, *Scattering of electromagnetic waves: Advanced topics*. John Wiley & Sons, 2001.

45. **Konings, A. G.**, **D. Entekhabi**, **M. Moghaddam**, and **S. S. Saatchi** (2014). The effect of variable soil moisture profiles on p-band backscatter. *IEEE Transactions on Geoscience and Remote Sensing*, **52**(10), 6315–6325.

46. **Li, K.-C.** (1991). Sliced inverse regression for dimension reduction. *Journal of the American Statistical Association*, **86**(414), 316–327.

47. **Ma, C.**, **X. Li**, and **K.-S. Chen** (2019). The discrepancy between backscattering model simulations and radar observations caused by scaling issues: An uncertainty analysis. *IEEE Transactions on Geoscience and Remote Sensing*.

48. **Moghaddam, M.**, **S. Saatchi**, and **R. H. Cuenca** (2000). Estimating subcanopy soil moisture with radar. *Journal of Geophysical Research: Atmospheres*, **105**(D11), 14899–14911.

49. **Narvekar, P. S.**, **D. Entekhabi**, **S.-B. Kim**, and **E. G. Njoku** (2015). Soil moisture retrieval using l-band radar observations. *IEEE Transactions on Geoscience and Remote Sensing*, **53**(6), 3492–3506.

50. **Njoku, E. G.** and **L. Li** (1999). Retrieval of land surface parameters using passive microwave measurements at 6-18 ghz. *IEEE Transactions on Geoscience and Remote Sensing*, **37**(1), 79–93.

51. **Oh, Y.**, **K. Sarabandi**, and **F. T. Ulaby** (1992). An empirical model and an inversion technique for radar scattering from bare soil surfaces. *IEEE transactions on Geoscience and Remote Sensing*, **30**(2), 370–381.

52. **Ouellette, J. D.**, **J. T. Johnson**, **A. Balenzano**, **F. Mattia**, **G. Satalino**, **S.-B. Kim**, **R. S. Dunbar**, **A. Colliander**, **M. H. Cosh**, **T. G. Caldwell**, *et al.* (2017). A time-series approach to estimating soil moisture from vegetated surfaces using l-band radar backscatter. *IEEE Transactions on Geoscience and Remote Sensing*, **55**(6), 3186–3193.

53. **Peake, W.** and **T. Oliver** (1971). The response of terrestrial surfaces at microwave frequencies. Technical report, OHIO STATE UNIV COLUMBUS ELECTROSCIENCE LAB.

54. **Peplinski, N. R.**, **F. T. Ulaby**, and **M. C. Dobson** (1995). Dielectric properties of soils in the 0.3-1.3-ghz range. *IEEE Transactions on Geoscience and Remote Sensing*, **33**(3), 803–807.

55. **Quesney, A.**, **S. Le Hégarat-Mascle**, **O. Taconet**, **D. Vidal-Madjar**, **J. Wigneron**, **C. Loumagne**, and **M. Normand** (2000). Estimation of watershed soil moisture index from ers/sar data. *Remote sensing of environment*, **72**(3), 290–303.

56. **Rice, S. O.** (1951). Reflection of electromagnetic waves from slightly rough surfaces. *Communications on pure and applied mathematics*, **4**(2-3), 351–378.

57. **Rodríguez-Fernández, N. J.**, **F. Aires**, **P. Richaume**, **Y. H. Kerr**, **C. Prigent**, **J. Kolassa**, **F. Cabot**, **C. Jimenez**, **A. Mahmoodi**, and **M. Drusch** (2015). Soil moisture retrieval using neural networks: Application to smos. *IEEE Transactions on Geoscience and Remote Sensing*, **53**(11), 5991–6007.

58. **Rosen, P. A.**, **S. Hensley**, **K. Wheeler**, **G. Sadowy**, **T. Miller**, **S. Shaffer**, **R. Muellerschoen**, **C. Jones**, **H. Zebker**, and **S. Madsen**, Uavsar: A new nasa airborne sar system for science and technology research. *In 2006 IEEE Conference on Radar*. IEEE, 2006.

59. **Rosen, P. A.**, **Y. Kim**, **R. Kumar**, **T. Misra**, **R. Bhan**, and **V. R. Sagi**, Global persistent sar sampling with the nasa-isro sar (nisar) mission. *In 2017 IEEE Radar Conference (RadarConf)*. IEEE, 2017.

60. **Sancer, M.** (1969). Shadow-corrected electromagnetic scattering from a randomly rough surface. *IEEE Transactions on Antennas and Propagation*, **17**(5), 577–585.

61. **Schneider, K.** and **N. Oppelt**, The determination of mesoscale soil moisture patterns with ers data. *In IGARSS'98. Sensing and Managing the Environment. 1998 IEEE International Geoscience and Remote Sensing. Symposium Proceedings.(Cat. No. 98CH36174)*, volume 4. IEEE, 1998.

62. **Shi, J.**, **J. Wang**, **A. Y. Hsu**, **P. E. O'Neill**, and **E. T. Engman** (1997). Estimation of bare surface soil moisture and surface roughness parameter using l-band sar image data. *IEEE Transactions on Geoscience and Remote Sensing*, **35**(5), 1254–1266.

63. **Tabatabaeenejad, A.**, **M. Burgin**, **X. Duan**, and **M. Moghaddam** (2014). P-band radar retrieval of subsurface soil moisture profile as a second-order polynomial: First airmoss results. *IEEE Transactions on Geoscience and Remote Sensing*, **53**(2), 645–658.

64. **Topp, G. C.**, **J. Davis**, and **A. P. Annan** (1980). Electromagnetic determination of soil water content: Measurements in coaxial transmission lines. *Water resources research*, **16**(3), 574–582.

65. **Tsang, L.**, **J. A. Kong**, and **R. T. Shin** (1985). Theory of microwave remote sensing.

66. **Ulaby, F.** (1974). Radar measurement of soil moisture content. *IEEE Transactions on Antennas and propagation*, **22**(2), 257–265.

67. **Ulaby, F. T.** (1982). Microwave remote sensing active and passive. *Rader remote sensing and surface scattering and emission theory*, 848–902.

68. **Ulaby, F. T.** (2014). COMPUTER CODES - MICROWAVE RADAR AND RADIOMETRIC REMOTE SENSING. `http://mrs.eecs.umich.edu/codes/`.

69. **Ulaby, F. T.** and **M. A. El-Rayes** (1987). Microwave dielectric spectrum of vegetation-part ii: Dual-dispersion model. *IEEE Transactions on Geoscience and Remote Sensing*, (5), 550–557.

70. **Ulaby, F. T.**, **D. G. Long**, **W. J. Blackwell**, **C. Elachi**, **A. K. Fung**, **C. Ruf**, **K. Sarabandi**, **H. A. Zebker**, and **J. Van Zyl**, *Microwave radar and radiometric remote sensing*, volume 4. University of Michigan Press Ann Arbor, 2014.

71. **Ulaby, F. T.**, **R. K. Moore**, and **A. K. Fung** (1981). Microwave remote sensing: Active and passive. volume 1-microwave remote sensing fundamentals and radiometry.

72. **Ulaby, F. T.**, **M. Whitt**, and **M. Dobson** (1990). Measuring the propagation properties of a forest canopy using a polarimetric scatterometer. *IEEE transactions on antennas and propagation*, **38**(2), 251–258.

73. **van Zyl, J. J.**, *Synthetic aperture radar polarimetry*, volume 2. John Wiley & Sons, 2011.

74. **Voronovich, A.** (1994). Small-slope approximation for electromagnetic wave scattering at a rough interface of two dielectric half-spaces. *Waves in random media*, **4**(3), 337–368.

75. **Wagner, W.** and **K. Scipal** (2000). Large-scale soil moisture mapping in western africa using the ers scatterometer. *IEEE Transactions on Geoscience and Remote Sensing*, **38**(4), 1777–1782.

76. **Wang, J. R.**, **E. T. Engmen**, **J. C. Shiue**, **M. Rusek**, and **C. Steinmeier** (1986). The sir-b observations of microwave backscatter dependence on soil moisture, surface roughness, and vegetation covers. *IEEE Transactions on Geoscience and Remote Sensing*, (4), 510–516.

77. **Wang, T.**, **J. Liang**, and **X. Liu** (2019). Soil moisture retrieval algorithm based on tfa and cnn. *IEEE Access*, **7**, 597–604. ISSN 2169-3536.

78. **Wu, T.-D.** and **K.-S. Chen** (2004). A reappraisal of the validity of the iem model for backscattering from rough surfaces. *IEEE Transactions on Geoscience and Remote Sensing*, **42**(4), 743–753.

79. **Yang, Y.** and **K.-S. Chen** (2019). Full-polarization bistatic scattering from an inhomogeneous rough surface. *IEEE Transactions on Geoscience and Remote Sensing*.

80. **Yang, Y.**, **K.-S. Chen**, **L. Tsang**, and **L. Yu** (2017). Depolarized backscattering of rough surface by aiem model. *IEEE Journal of Selected Topics in Applied Earth Observations and Remote Sensing*, **10**(11), 4740–4752.

81. **Zribi, M.** and **M. Dechambre** (2003). A new empirical model to retrieve soil moisture and roughness from c-band radar data. *Remote Sensing of Environment*, **84**(1), 42–52.

LIST OF PAPERS BASED ON THESIS

Manuscripts under Preparation

1. **Siddhant Gautam**, Dharmendra K Pandey, Shivani Tyagi, Uday K Khankhoje, "**Soil Moisture Retrieval from Multi-Frequency Multi-Polarization SAR Data Using a Sliced Regression Inversion Technique**"

Peer Reviewed Conferences

1. **Gautam, S.**, S. V. Chidambaram, N. Gunturu, and U. K. Khankhoje, **Retrieval of soil moisture using sliced regression inversion technique**. In 2019 PhotonIcs and Electromagnetics Research Symposium-Spring (PIERS-Spring). IEEE, 2019